

Warping of Radar Data into Camera Image for Cross-Modal Supervision in Automotive Applications

Christopher Grimm, Tai Fei, Ernst Warsitz, Ridha Farhoud, Tobias Breddermann, Reinhold Haeb-Umbach

Abstract—In this paper, we present a novel framework to project automotive radar range-Doppler (RD) spectrum into camera image. The utilized warping operation is designed to be fully differentiable, which allows error backpropagation through the operation. This enables the training of neural networks (NN) operating exclusively on RD spectrum by utilizing labels provided from camera vision models. As the warping operation relies on accurate scene flow, additionally, we present a novel scene flow estimation algorithm fed from camera, lidar and radar, enabling us to improve the accuracy of the warping operation. We demonstrate the framework in multiple applications like direction-of-arrival (DoA) estimation, target detection, semantic segmentation and estimation of radar power from camera data. Extensive evaluations have been carried out for the DoA application and suggest superior quality for NN based estimators compared to classical estimators. The novel scene flow estimation approach is benchmarked against state-of-the-art scene flow algorithms and outperforms them by roughly a third.

Index Terms—Automotive radar, neural network, Lidar, virtual testing, Direction-of-Arrival, cross-modal supervision

I. INTRODUCTION

In the past decade, neural network (NN) based algorithms have proven superiority in comparison to classical machine learning algorithms in several applications [1], [2], [3]. One significant challenge in training NN based algorithms, comes from the supervision principle, where sufficient labeled data must be provided in order to adapt the large amount of network parameters. In case of frequency level —we will use frequency level, low-level and RD spectrum interchangeably— automotive FMCW radar signal processing this becomes a significant practical problem, as the input data is not native to human and thus cannot be labeled manually as e.g. camera images.

In this paper, we solve this problem by automatically generating high-quality labels from a reference systems consisting of camera, lidar and state-of-the-art vision-models. This task is challenging, as the reference system natively operates in a different measurement space compared to radar and thus labels cannot be shared trivially to supervise radar training. We expand the measurement space of the reference system, to cover the measurement space of the radar, by estimating Doppler information and warp RD spectrum data of the radar into camera images.

Christopher Grimm, Tai Fei, Ernst Warsitz, Ridha Farhoud and Tobias Breddermann are employees of Hella GmbH & Co. KGaA & Co., 59555 Lippstadt, Germany e-mail: {christopher.grimm, tai.fei, ernst.warsitz, ridha.farhoud, tobias.breddermann}@hella.com

Reinhold Haeb-Umbach is with the Department of Communication Engineering, University of Paderborn, 33098 Paderborn, Germany e-mail: haeb@nt.uni-paderborn.de.

This leverages the application of supervision for algorithms operating on RD spectrum by comparing inference results to the labels of the reference system. Because the warping function is designed to be fully differentiable, the warping operation can then be integrated into the backpropagation process during the training phase. The proposed framework has been summarized in Fig. 1. It can be viewed as a universal framework for cross-modal supervision of NN operating on FMCW radar data.

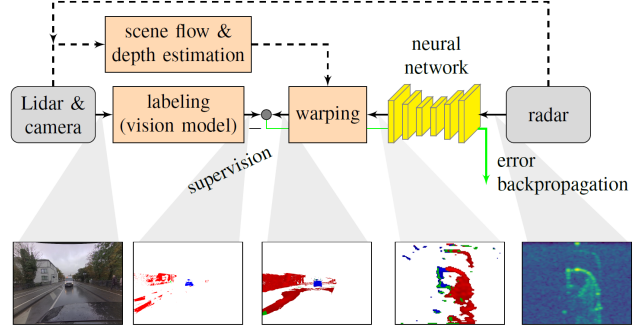


Figure 1. Overview of the model pipeline: Lidar and camera provide sensor readings to the vision model which automatically generates labels in the camera image. At the same time, the radar sensor reading is processed by a NN and warped from RD spectrum into the camera image domain. The residue between the generated label and the warped NN prediction is calculated and then backpropagated through the warping operation and the NN for parameter adjustment (green arrow). The lower images represent signal vectors in case of semantic segmentation application. From left to right: RGB image, reference semantic mask (only relevant pixels shown), predicted semantic mask warped into camera image, predicted semantic mask in RD-spectrum, RD-map

We demonstrate this framework extensively in the application of radar based Direction-of-Arrival (DoA) estimation including qualitative and quantitative examples. Additionally, the proposed approach is also verified given qualitative examples for the applications of target detection, semantic segmentation and power estimation from camera.

This paper comprises the following novelties:

- state-of-the-art scene flow estimation by incorporation of frequency level radar data
- automatic label generation for frequency level radar data by utilizing labels from camera vision models
- definition of robust learning strategies to enable training of NNs in real world data for multiple radar applications, especially considering label noise.

The remainder of this paper is organized as follows. Sec. II summarizes related work in the field of automotive dataset generation and recent NN applications for radar DoA estimations. Sec. III provides a glance into our vehicle setup, including utilized sensors and description of basic sensor calibration.

Sec. IV describes the utilized Doppler estimation algorithm for the reference system, which is required by the warping operation (Sec. V). In Sec. VI, training objectives for the NNs and network architectures are given as well as techniques on how to make training more robust against reference label errors. In Sec. VII the NN based DoA estimators accuracies are evaluated. The conclusions are drawn in Sec. VIII.

II. RELATED WORK

This section is divided into two subsections. The first describes related work in the field of automotive datasets and automatic label generation, while the second segment provides insight into recent NN techniques for radar based DoA estimation.

1) *Datasets:* In 2012, Geiger *et al.* [4] introduced the famous KITTI dataset. The development and publication of this dataset was motivated by the declared intention to enforce the development of computer vision for autonomous driving. At that time, state-of-the-art algorithms were defined in laboratory conditions, and performed poorly, when first applied to automotive applications [5]. For the collection of camera, lidar and GPS data, the authors prepared their autonomous driving platform and recorded approx. 40 km of data in real world driving scenarios around Karlsruhe, Germany. Starting with benchmarks for stereo vision, optical flow, visual odometry and 3D object detection, in which ground truth was provided either by sensor fusion or in case of object detection by human labelers, the benchmark nowadays has been extended for applications such as depth completion of sparse depth measurements, semantic segmentation and scene flow [6]. Despite the pioneering work of the authors and the ongoing evolution of the dataset, additional sensor such as automotive radar have not been adopted into the dataset, and this dataset is accordingly not applicable to automotive radar sensors. In fact, object detection ground truth is mainly available in the cameras field of view (FoV). Thus, the dataset is primarily targeted towards camera vision applications.

In 2019 Caeser *et al.* has proposed the nuScenes dataset to tackle the availability of multimodal datasets, which incorporated sensor data from multiple cameras, lidar and radars. The ground truth in this dataset was mostly acquired by professional human labelers, for instance in the form of 3D object bounding boxes. The dataset currently contains approx. 242 km of driving data Boston, USA and Singapore. The radar data is given as a pointcloud consisting of radar detections, in which each point has an assigned position and velocity. From the perspective of radar signal processing, the radar signals in this dataset are already on high level, and frequency level data is missing. Accordingly, it is barely applicable to the frequency level signal processing see e.g. [7].

Similar conclusion applies to the dataset provided in [8].

Other relevant automotive datasets can be found e.g., in [9], [10] which engage in creating large and densely annotated camera data only.

Due to the requirement for large automotive datasets, recently more and more synthetic datasets have appeared [11], [12], [13]. These datasets provide synthesized camera images

as well as detailed ground truth from the synthetic environment. To be beneficial for radar development, these datasets have to be extended to provide synthesized radar data as well. It is important, that synthetic data is required to imitate real world data with high quality in order to achieve comparable application results in both domains, see e.g., [14].

Bühren *et al.* [15] have synthesized radar targets from traffic simulations or databases. However, the simulation was carried out on high level radar data. As already mentioned above, it does not help in developing frequency level signal processing algorithm developments.

In [16] the authors proposed a DGPS based reference system for radar target evaluation. Although very precise, reference data is only provided for traffic users equipped with this reference system. Thus, the acquisition of large datasets is practically impossible.

In 2018 Schult [17] presented a method to generate reference RD spectrums from lidar data, in which vehicles are detected in the lidars point cloud and tracked over time. However, the reference RD-maps are very sparse, since a) only a reference for vehicles was given and b) vehicles are modeled as a single point reflectors.

In 2019 Major *et al.* [18] trained deep-learning object detection operating on range-azimuth-Doppler spectrum in real world driving scenarios. The radar data is transformed from polar-coordinates into Cartesian coordinate system of the reference lidar sensor, in which the object labels are presented to the network. However, the Cartesian coordinate transformation relies on accurate azimuth resolution of the radar itself, which we found not to be the case for state-of-the-art series production radar sensors for ADAS applications.

In [19] the authors showcased deep-learning based object detection trained on simulated RD-maps via raytracing. Different driving scenarios were simulated and a trained object detector was able to achieve decent performance in the test data. The test data originated from the same raytracing tool and thus performance and real world data remains unknown.

In [20], [21] the authors labeled radar target clusters by fusion of camera images, lidar pings and radar targets with the help of state-of-the-art perception models and achieved 72 % classification accuracy compared to humans with a significant reduction in label time effort. They achieved an 0.48 m average translational error in nuScenes object detection benchmark. However, as our aim is to automate label RD spectrum data, this approach is also not feasible here.

The motivation of this paper leads to build a dataset of frequency level radar data as well as application specific ground truth, which can assist the development and evaluation of signal processing algorithms in this preceding processing step.

2) *Direction-of-Arrival estimation via radar:* Commonly refereed classical methods for DoA radar application are phase-monopulse or Bartlett beamforming, see e.g. [22], [23]. Recent NN based approaches were presented [24], [25], [26]. The authors installed a radar-under-test on an azimuth positioner in an anechoic chamber and placed a corner reflector 1.5 m in front of the sensor. Measurement data from the radar sensor was acquired at different azimuth orientations. As the

target position was known, it served as ground truth label for multi-layer perceptron (MLP) training. The MLP was trained to estimate DoA for up to two targets, and achieved similar performance as classical algorithms for instance Deterministic Maximum Likelihood, while being significantly faster in inference. As the data collected in anechoic chamber might differ from data obtained in real world traffic scenarios, we will focus on training and evaluating NNs in the latter scenarios.

III. DATA ACQUISITION SYSTEM AND SENSOR CALIBRATION

To gather real world sensor data from driving scenarios, we equipped a car with a 77 GHz Hella radar sensors, which acquires raw data, forms RD spectrum in the first processing step and shares them to an in-vehicle recording PC. The radar sensor is mounted at the rear right corner and behind the bumper, as illustrated in Fig. 2. The utilized reference sensor system consisting of 2 Velodyne VLP-32C lidar scanners [27] and a camera array (2 FirstSensor DC3C-1-E4P-105 [28]) is mounted on a luggage rack on top of the vehicle. The camera array is able to record a continuous videotream at 30 FPS. In order to sample the surrounding more densely, our system is equipped with two lidar sensors, which are mounted with different orientations on the vehicle. Together they provide a denser point-cloud in the radars FoV, see Fig. 5. In order to cover the entire radar FoV (azimuth: 135°, elevation: 22°), two cameras (azimuth: $\approx 104^\circ$) with overlapping FoVs were used. The Differential-GPS with inertial navigation system (DGPS-INS) of type GeneSys ADMA-G-Pro+ [29] is used as a reference sensor for precise vehicle over ground motion.

The driving trajectory for this dataset is illustrated in Fig. 2 and contains mostly urban environment over a period of approx. 1 h driving, 36000 frames or approx. 7 billion samples on pixel level.

For the sake of convenience, we will use the notation $C_1, C_2, D, E, L_1, L_2, R$ to indicate coordinates relative to camera 1 & 2, DGPS-INS, ego-vehicle, lidar 1 & 2 as well as the radar unit under test. As each sensor provides data in its own coordinate system (COOS), the data needs to be transformed before being processed in coherence. Two substantial tasks are performed to ensure geometric data alignments between sensor measurements, namely geometric and temporal calibration, described in the next subsection. Geometric calibration determines the rigid body transformation between sensor pairs $i, j \in \{E, C, R, L, D\}$ by a rotation ${}^i\mathbf{R}_j \in \mathbb{R}^{3 \times 3}$ (Euler-rotational matrix) and translational vector ${}^i\mathbf{t}_j \in \mathbb{R}^{3 \times 1}$. Data points given in Cartesian COOS j as $\mathbf{x}_j = [x_{j,x}, x_{j,y}, x_{j,z}]^T$ can thus be described in other sensors coordinates i . As 7 COOSs are drawn in Fig. 2, 6 transformations describe the system:

$$\mathbf{x}_E = {}^E\mathbf{R}_{L1}\mathbf{x}_{L1} + {}^E\mathbf{t}_{L1} \quad (1a)$$

$$\mathbf{x}_E = {}^E\mathbf{R}_{L2}\mathbf{x}_{L2} + {}^E\mathbf{t}_{L2} \quad (1b)$$

$$\mathbf{x}_{C1} = {}^{C1}\mathbf{R}_{L1}\mathbf{x}_{L1} + {}^{C1}\mathbf{t}_{L1} \quad (1c)$$

$$\mathbf{x}_{C2} = {}^{C2}\mathbf{R}_{L1}\mathbf{x}_{L1} + {}^{C2}\mathbf{t}_{L1} \quad (1d)$$

$$\mathbf{x}_R = {}^R\mathbf{R}_E(\mathbf{x}_E + {}^R\mathbf{t}_E) \quad (1e)$$

$$\mathbf{x}_E = {}^E\mathbf{R}_D\mathbf{x}_D + {}^E\mathbf{t}_D. \quad (1f)$$

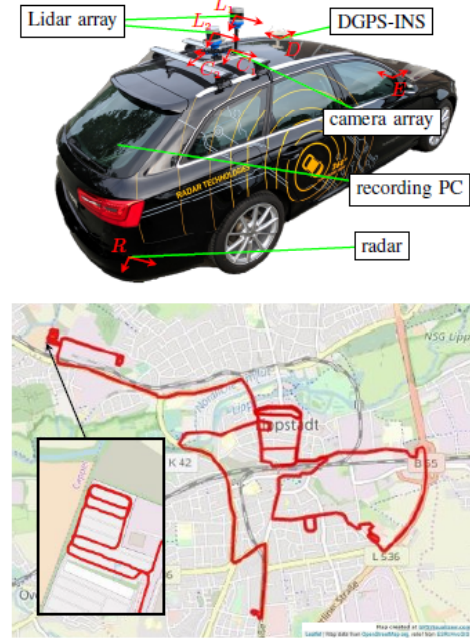


Figure 2. **Dataset overview:** Top-to-bottom: vehicle sensor configuration and dataset trajectory with magnified scene flow evaluation area.

The tuples $({}^E\mathbf{R}_{L1}, {}^E\mathbf{t}_{L1})$ and $({}^E\mathbf{R}_{L2}, {}^E\mathbf{t}_{L2})$ have been estimated via [30]. The tuples $({}^{C1}\mathbf{R}_{L1}, {}^{C1}\mathbf{t}_{L1})$ and $({}^{C2}\mathbf{R}_{L1}, {}^{C2}\mathbf{t}_{L1})$ have been extracted from sensor mounting parameters, hence the cameras were mounted directly to the lidar sensors. Radar position relative to vehicle $({}^R\mathbf{R}_E, {}^R\mathbf{t}_E)$ was measured via [31], including intrinsic calibration. The DGPS-INS position $({}^E\mathbf{R}_D, {}^E\mathbf{t}_D)$ has been measured geometrically via measuring tape.

The output of camera is an image, and angular information is coded in the image pixels \mathbf{p}_i for camera $i \in \{1, 2\}$. Thus, this information has to be converted into coordinates in \mathbf{x}_{C1} and \mathbf{x}_{C2} . This is done by applying a camera-pinhole model from Eq. 2b and 2c with the intrinsic parameters focal lengths $\{f_{x1}, f_{y1}, f_{x2}, f_{y2}\}$ and principal points $\{c_{x1}, c_{y1}, c_{x2}, c_{y2}\}$, estimated via [4]

$$\mathbf{p}_i = [u_i, v_i]^T \quad (2a)$$

$$x_{ci,x} = \frac{u_i - c_{xi}}{f_{xi}} x_{ci,z} \quad (2b)$$

$$x_{ci,y} = \frac{v_i - c_{yi}}{f_{yi}} x_{ci,z}. \quad (2c)$$

As the remainder of this paper applies to both cameras, further on, we will discard the camera index i for the sake of simplicity.

2) *Temporal calibration:* The angular resolution of the camera image and thus the native resolution of our reference sensor is approx. 0.16° . However, parasitic exposure time differences between camera and lidar lead to degradation of the effective resolution and motivates the incorporation of temporal calibration.

The sensor data streams were stamped with the recording PC's time at the moment of receipt. Assuming constant propagation delay on the sensor interfaces, an empirically determined time shift per sensor was added to the receipt

timestamp. For every radar cycle, the closest data package in time from the other sensors were utilized as corresponding reference. The remaining time difference between camera and lidar is $\Delta t_{\text{lidar} \rightarrow \text{camera}} \in [-\frac{1}{2\text{FPS}_{\text{camera}}}, \frac{1}{2\text{FPS}_{\text{camera}}}]$. Unfortunately, the utilized camera exposure could not be triggered on time, when the lidars lasers hover over the cameras visual axis like in [4], [32], [33]. Thus, an exposure time difference between camera and lidar is present. This time difference is corrected algorithmically via [34] to ensure proper temporal calibration between the sensors and their underlying data. One exemplary outcome of this temporal calibration can be seen in Fig. 3. With exposure time compensation, the color coded lidar depth measurements align with the image content better, which is immediately recognizable at the location of the tree in the image background.

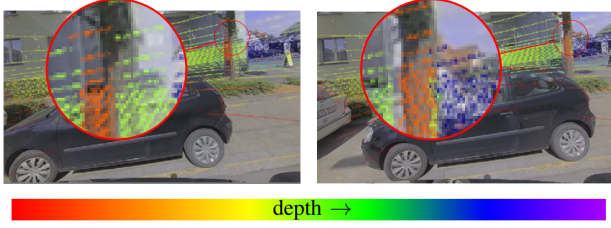


Figure 3. **Geometrical alignment of lidar and camera measurements between similar scenes:** Left: after geometrical calibration only, right: after geometrical and temporal calibration.

IV. NOVEL SCENE FLOW ESTIMATION APPROACH

In order to warp the radar RD data into camera image, as shown in Fig. 1, we first estimate the 3-D velocity for every pixel in the camera images. This process is commonly referred as scene flow estimation.

In [35] a scene flow algorithm called deep rigid instance scene flow (DRISF) was proposed, which holds state-of-the-art performance on KITTI dataset at the time of development of this paper. The idea is, that the overall scene flow can be formed by estimating the 3-D motion of each actor individually. DRISF is fed with visual cues and obtains scene flow by applying a Gauss-Newton (GN) solver on formulated energy terms.

As we found the accuracy of DRISF is insufficient to achieve a satisfactory warp performance, we hereby propose an extended approach called deep rigid instance scene flow with radar (DRISFwR) which incorporates RD spectrum data into DRISF. This radar specific adaptation is depicted in Fig. 4.

It does not only help in reducing scene flow errors, but integrates automatic alignment of scene flow estimation to radar data. Advantageously, the manual labeling effort spent in the detection of scene flow errors in our test dataset was reduced, more in Sec. VII-B. Furthermore, we incorporate precise ego-motion from DGPS-INS into the algorithm to achieve accurate estimations of static background scene flow.

In this section, we describe the input features for DRISFwR, define required pixel subsets, the process of static background scene flow estimation and the required adaptation of energy formulation for foreground objects.

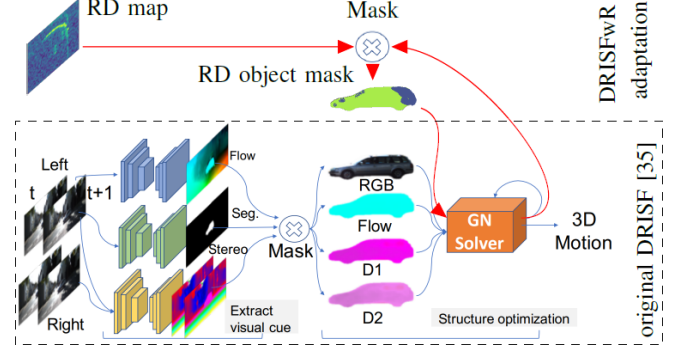


Figure 4. **DRISFwR overview:** Adapted from [35], the original DRISF approach is drawn in the dashed rectangle. Our DRISFwR adaptation on top, implies the red drawn path. After each GN solver iteration, the RD object mask is updated and used for next iteration.

A. Input features

Four types of visual cues are exploited: instance segmentation, optical flow, dense depth and RD-map.

Instance Segmentation: Semantic instance segmentation is produced via mask_rcnn_inception_v2_coco from Tensorflow model zoo [36]. This NN was trained on the COCO dataset and selected here for its good accuracy and fast inference time. During inference, semantic object masks \mathcal{S} are generated as well as object classes. Since the utilized network is not specifically tailored for automotive classes, we retain only the following five relevant classes: pedestrian, car, truck, bicycle or bike.

Optical Flow: For optical flow calculation between two adjacent RGB frames, HD³-Flow [37] has been applied. It learns probabilistic pixel correspondences to provide optical flow confidence on the pixel level and achieves state-of-the-art results in KITTI dataset. The flow masks are summarized in \mathcal{F} .

Stereo / Dense depth: In DRISF [35], Ma *et al.* obtained depth estimation based on the stereo camera setup of the KITTI dataset. As our sensor setup does not provide stereo cameras, we provide dense depth \mathcal{D} by utilizing sparse depth measurements $\mathcal{D}_{\text{sparse}} := \{\mathbf{p} \mid \mathbf{p} \in \text{lidar}\}$ from lidars and pack it with the help of mono-cameras. This process is called depth completion with lots of research done in [38], [4]. We utilized the algorithm proposed by [39] which solves depth completion via Markov-Random-Field and that requires no adjustment to our sensor setup. The algorithm projects the sparse lidar depth measurements onto the camera image, with the help of Eq. 1c, 2b and 2c, and propagates the depth values from lidar occupied pixels into regions with similar brightness values, whilst enforcing 2nd order smoothness in depth. An example of depth completed lidar depth measurements can be seen in Fig. 5.

RD-map: As a substantially new cue in comparison to DRISF, radar RD-map \mathcal{RD} , which is RD power spectrum, is provided as a direct velocity measurement source from the scene. \mathcal{RD} is computed from the RD spectra $\mathcal{U}_i \in \mathbb{C}$ per receive antenna i ,

$$\mathcal{RD} = \sum_{i=3} 20 \log_{10} \|\mathcal{U}_i\|_2. \quad (3)$$

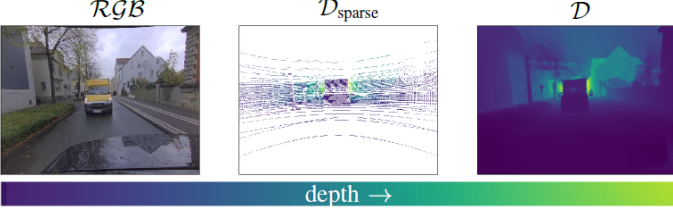


Figure 5. **Depth completion results:** Left-to-right: RGB image, sparse depth, dense depth obtained by depth completion.

For further information please refer to [40]. Apparent in these RD-maps is the power of reflections in the RD spectrum according to its relative range and radial velocity relative to the radar.

B. Subset definitions

All pixels \mathbf{p} classified as one of the classes form the set $\mathcal{P}_{\text{fg}} := \{\mathbf{p} \mid \mathbf{p} \in \text{pedestrian, car, truck, bicycle, motorbike}\}$.

As the radar does not cover the entire FoV from the cameras, the set $\mathcal{P}_{\text{radar}}$ captures all pixels covered by the radars FoV

$$\mathcal{P}_{\text{radar}} := \left\{ \mathbf{p}(\mathbf{x}_R) \mid |\phi(\mathbf{x}_R)| \leq \frac{135^\circ}{2} \wedge |\theta(\mathbf{x}_R)| \leq \frac{22^\circ}{2} \right\}, \text{ where}$$

$$\phi(\mathbf{x}_R) = \tan^{-1}(x_{R,x}, x_{R,y}), \theta(\mathbf{x}_R) = \tan^{-1}(x_{R,x}, x_{R,z}). \quad (4)$$

To mitigate the effect of errors in instance segmentation, we perform further object clustering on each instance pointcloud via DBSCAN [41]. Thereby points which have spatial distance larger than 0.3 m from the closest point in the cluster i are classified as outliers. The set \mathcal{P}_i describes the remaining pixels consent to the DBSCAN criterion and visible to the radar,

$$\mathcal{P}_i := \left\{ \mathbf{p} \mid \mathbf{p} \in \text{DBSCAN}(\mathbf{p}) \wedge \mathbf{p} \mid \mathbf{p} \in \mathcal{P}_{\text{radar}} \right\}. \quad (5)$$

For the sake of simplicity, let $\mathcal{I} = \{\mathcal{RG}\mathcal{B}^0, \mathcal{RG}\mathcal{B}^1, \mathcal{D}^0, \mathcal{D}^1, \mathcal{S}^0, \mathcal{F}, \mathcal{RD}\}$.

C. Motion formulation

We superimpose the overall scene flow $\xi = [\xi_x, \xi_y, \xi_z]^T$ from background ξ_{bg} and foreground motion ξ_{fg} ,

$$\xi = \xi_{bg} + \xi_{fg}. \quad (6)$$

The background motion encodes relative motion of the ego-motion over ground and is applied to all pixels. Foreground motion, is the motion of objects over ground. Similar to DRISF foreground motion is obtained only for pixels in \mathcal{S}_{fg} . Diverging from DRISF, the foreground motion is encoded in 3 translational motion parameters instead of 6 (3 rotational + 3 translational). No empirical investigation on the effect of this simplification has been carried out and is justified here, by assuming small objects and rotational speeds of foreground objects, similar to Eq. 7. Motion of the background highly depends on the motion of the ego-vehicle itself and rotation cannot be neglected, since, even when the ego-vehicles rotations is small, scene flow can be high for objects which are far away, see Eq. 7-9a. As the sensors obtain data with given sample period ($T = 0.1$ s), we introduce k as an indication for discrete sample time kT .

Background motion formulation: As background motion, we understand the relative 3-D motion of the environment induced by the movement of the ego-vehicle over ground. The position of a stationary point $\mathbf{x}_E(\mathbf{p})$ at timestep k can be predicted for timestep $k+1$ as

$$\mathbf{x}'_E(\mathbf{p}) = \mathbf{R}_{E,bg} \left(\mathbf{x}_E(\mathbf{p}) + \mathbf{x}_{RA} \right) - \mathbf{x}_{RA} - \mathbf{t}_{E,bg}, \quad (7)$$

in which $\mathbf{R}_{E,bg}$ and $\mathbf{t}_{E,bg}$ describe the rotation and translation of the ego-vehicle over ground obtained by DGPS-INS. Before rotating, points given in E are shifted onto the rear axle of the ego-vehicle via \mathbf{x}_{RA} , according to the Ackermann vehicle model [42], which assumes that vehicles yaw around their rear axle. Since we observed this to be slightly inaccurate — for speed evaluation, the inter frame positional error has to be within the millimeter scale — \mathbf{R}_{rot} and \mathbf{t}_{bg} have to be refined via camera motion. A similar observation has been described in [6] with a proposed algorithm. Background scene flow in camera coordinates is thus computed as

$$\xi_{bg} = \mathbf{x}'_C(\mathbf{p}) - \mathbf{x}_C(\mathbf{p}), \quad (8)$$

and can be derived via substitution of Eq. 1a-1f into Eq. 7

$$\mathbf{x}'_C(\mathbf{p}) = \mathbf{R}_{C,bg} \mathbf{x}_C(\mathbf{p}) + \mathbf{t}_{C,bg} \quad (9a)$$

$$\mathbf{R}_{C,bg}(k) = {}^C \mathbf{R}_L^E \mathbf{R}_L^{-1} {}^E \mathbf{R}_{E,bg} {}^E \mathbf{R}_L {}^C \mathbf{R}_L^{-1} \quad (9b)$$

$$\begin{aligned} \mathbf{t}_{C,bg} = & \left(\mathbf{I} - \mathbf{R}_{C,bg} \right) {}^C \mathbf{t}_L + {}^C \mathbf{R}_L {}^E \mathbf{R}_L^{-1} \left(\mathbf{R}_{E,bg}^T - \mathbf{I} \right) {}^E \mathbf{t}_L \\ & + {}^C \mathbf{R}_L {}^E \mathbf{R}_L^{-1} \left(\mathbf{I} - \mathbf{R}_{E,bg} \right) \mathbf{x}_{RA} - {}^C \mathbf{R}_L {}^E \mathbf{R}_L^{-1} \mathbf{t}_{E,bg}. \end{aligned} \quad (9c)$$

The background motion $\xi_{bg}(\mathbf{p})$ for each camera pixel is thus estimated by obtaining current position $\mathbf{x}_C(\mathbf{p})$ from dense depth image and ego-motion via Eq. 2b, 2c and 8-9c.

Foreground motion formulation: In DRISFwR, a radar specific energy term is added to the energy formulation of DRISF, as shown in Eq. 35

$$\begin{aligned} \min_{\xi} \left\{ \underbrace{\lambda_{\text{photo}} E_{\text{photo}}(\xi; \mathcal{I}) + \lambda_{\text{rigid}} E_{\text{rigid}}(\xi; \mathcal{I}) + \lambda_{\text{flow}} E_{\text{flow}}(\xi; \mathcal{I})}_{\text{original DRISF}} + \right. \\ \left. \underbrace{\sum_{s_d=1}^3 \lambda_{\text{radar}, s_d} E_{\text{radar}}(\xi; \mathcal{I}, s_d)}_{\text{extension by DRISFwR}} \right\}. \end{aligned} \quad (10)$$

E_{photo} describes, how well the $\mathcal{RG}\mathcal{B}$ pixels from the object agree to those corresponding to $\mathcal{RG}\mathcal{B}$, with respect to ξ . E_{rigid} describes how well pixel positions (acquired from \mathcal{D}) agree in between frames with respect to ξ . The E_{flow} energy captures differences between \mathcal{F} and the obtained scene flow. For more detail about these energy terms, we refer the reader to the original DRISF paper, as we will focus on the radar specific extension here. The newly introduced E_{radar} energy captures how well ξ agrees to the relative velocity measured by radar, with the mathematical formulation following in Eq. 13b. The λ scale the influence of each energy term.

Minimization is performed by reformulation of Eq. 35 as an adaptive weighted sum of squares:

$$\xi^{(m+1)} = \underset{\xi}{\operatorname{argmin}} \sum_E \mathbf{W}(\xi^{(m)}) \mathbf{r}^T(\xi^{(m)}) \mathbf{r}(\xi^{(m)}), \quad (11)$$

with \mathbf{r} being the residual vector and \mathbf{W} the sample weight for the pixels corresponding to an instance. In each iteration m , the GN solver performs scene flow updates $\xi^{(m+1)} = \xi^{(m)} + \Delta\xi^{(m)}$ by computing

$$\Delta\xi^{(m)} = -(\mathbf{J}^T \mathbf{W} \mathbf{J})^{-1} \mathbf{J}^T \mathbf{W} \mathbf{r}, \quad (12)$$

with $\mathbf{J} = \frac{\partial r(\xi; \mathcal{I})}{\partial \xi}$ being the Jacobian of the residuals. All required terms are derived from the energy functions and change with m .

The radar specified energy is formulated as

$$E_{\text{radar}}(\xi; \mathcal{I}, s_d) = \sum_{\mathbf{p} \in P_i} \rho(r_{\text{radar}}(\xi, \mathbf{p}; \mathcal{I}, s_d)) \quad (13a)$$

$$r_{\text{radar}}(\xi, \mathbf{p}; \mathcal{I}, s_d) = \mathcal{RD}(|\mathbf{x}_R(\mathbf{p})|, v_R(\xi, \mathbf{p}), s_d) - \mathcal{RD}_{\text{target}}, \quad (13b)$$

where $\rho(r_{\text{radar}}) = (r_{\text{radar}}^2 + 10^{-6})^{0.45}$ (generalized Charbonnier penalty) is the robust fitting function which we adopt from original DRISF. The RD-map value at range $|\mathbf{x}_R|$ and relative velocity $v_R(\xi)$ seen from radar is $\mathcal{RD}(|\mathbf{x}_R|, v_R(\xi))$, whereas $\mathcal{RD}_{\text{target}}$ is the target value for the power and here parameterized to be the maximum value of the RD-map, which enforces scene flow maximizing objects RD-map value in its pixel vicinity. We found this behavior similar to what human labelers would expect. An update step is depicted in Fig. 6, whereas the RD energy value of two trailing vehicles shown in camera image increased reasonable. Note that the projection itself will be explained in Sec. V.

For the sake of simplicity, we will ignore to highlight dependencies of \mathbf{p} , except there, where we think it is mandatory for better understanding.

In order to update ξ iteratively and thus minimize the energy formulation, the Jacobian of r_{radar} is derived via chain rule as partial derivative with ξ :

$$\mathbf{J}_{\text{radar}} = \frac{\partial r_{\text{radar}}(\xi; \mathcal{I}, s_d)}{\partial \xi} = \frac{\partial \mathcal{RD}(\xi; \mathcal{I}, s_d)}{\partial v_R(\xi)} \frac{\partial v_R(\xi)}{\partial \xi_{\text{radar}}} \frac{\partial \xi_{\text{radar}}(\xi)}{\partial \xi}. \quad (14)$$

The first term on the right hand side represents the RD-map power dependency from relative radial velocity in form of image gradients and is illustrated in Fig. 6.

Since image gradients in RD-map are very steep, scale-space [43] is created by repeated Gaussian smoothing, max-pooling of \mathcal{RD} and bilinear up-sampling alongside the Doppler dimension. Smoothing is used to create even gradients and max-pooling enhances the receptive field of DRISFwR and allows object alignment in RD-map over wider velocity ranges. Upscaling is performed to keep bin resolution constant over scales, however, induce further content smoothing. Different scale levels s_d are respected in DRISFwR by accumulating their energy in Eq. 35. To prefer alignment on lower scales, energy weighting λ_{radar} , is bisected every scale s_d . Furthermore, to cope with aliasing effect in Doppler spectrum, copies of the radar spectra are concatenated in Doppler direction, see Fig. 6.

The second right hand side term from Eq. 14 can be derived via

$$v_r(\xi, \mathbf{p}) = \frac{\mathbf{x}_R^T}{|\mathbf{x}_R|} \xi_{\text{radar}}(\xi), \quad (15)$$

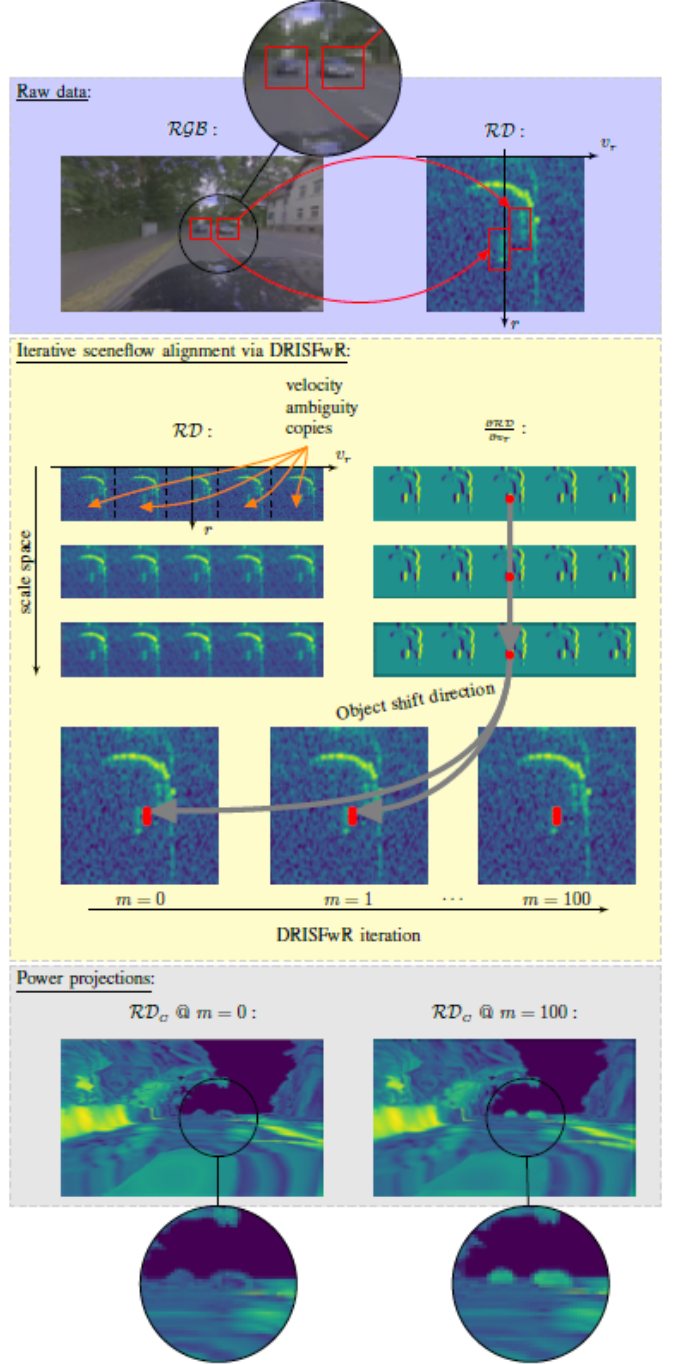


Figure 6. **Automatic scene flow alignment to Radar data via DRISFwR:** Top: RGB image and RD-map with two vehicles. Middle: Scale-space of radar data used in DRISFwR with energy & partial derivative. One object visualized in scalespace as red points. Repositioning via scene flow adjustment in consecutive DRISFwR update steps with gray arrows marking shift direction. Bottom: Power projections. After DRISFwR convergence, energy projection from RD-map is captured correctly for both vehicles

which is the scalar projection of the scene flow onto positional vector \mathbf{x}_r , both observed from radar perspective. Resulting in:

$$\frac{\partial v_r(\xi)}{\partial \xi_{\text{radar}}} = \frac{\mathbf{x}_R^T}{|\mathbf{x}_R|}. \quad (16)$$

As \mathbf{x}_R can be described by \mathbf{x}_C via reciprocally substitution of

Eq. 1a - 1f:

$$\mathbf{x}_R = {}^R\mathbf{R}_E \left({}^E\mathbf{R}_L {}^C\mathbf{R}_L^{-1} (\mathbf{x}_C - {}^C\mathbf{t}_L) + {}^E\mathbf{t}_L + {}^R\mathbf{t}_E \right), \quad (17)$$

the remaining term from Eq. 14 is derived from

$$\boldsymbol{\xi}_{\text{radar}} = \frac{\partial \mathbf{x}_R}{\partial t} = {}^R\mathbf{R}_E {}^E\mathbf{R}_L {}^C\mathbf{R}_L^{-1} \frac{\partial \mathbf{x}_C}{\partial t} = {}^R\mathbf{R}_E {}^E\mathbf{R}_L {}^C\mathbf{R}_L^{-1} \boldsymbol{\xi} = {}^R\mathbf{R}_C \boldsymbol{\xi}, \quad (18)$$

which transforms the scene flow from camera coordinates into radar coordinates via the rotational matrix ${}^R\mathbf{R}_C$, resulting in

$$\frac{\partial \boldsymbol{\xi}_{\text{radar}}}{\partial \boldsymbol{\xi}} = {}^R\mathbf{R}_C. \quad (19)$$

The adaptive weighting W_{radar} is derived as:

$$W_{\text{radar}} = \lambda_{\text{radar}} \frac{\partial^2 \rho}{\partial r_{\text{radar}}^2} = 0.45 \lambda_{\text{radar}} (r_{\text{radar}}^2 + 10^{-6})^{-0.55} \quad (20)$$

Now, the DIRSFwR Jacobian, residual and weighting matrix are the concatenation of the original DRISF (see [35]) ones paired with the radar specific ones:

$$\mathbf{J} = \begin{bmatrix} \mathbf{J}_{\text{DRISF}} \\ \mathbf{J}_{\text{radar}} \end{bmatrix} \quad (21a)$$

$$\mathbf{r} = \begin{bmatrix} \mathbf{r}_{\text{DRISF}} \\ r_{\text{radar}} \end{bmatrix} \quad (21b)$$

$$\mathbf{W} = \begin{bmatrix} \mathbf{W}_{\text{DRISF}} \\ W_{\text{radar}} \end{bmatrix}. \quad (21c)$$

GN iterations are stopped here once $\|\Delta \boldsymbol{\xi}\|_2 < 0.1$ mm. Typically this appeared after approx. 30 iterations but was stopped when convergence was not reached after 100 iterations.

V. WARPING FROM RADAR SPECTRA INTO CAMERA IMAGE

In the previous section, we described our process of generation per pixel scene flow as well as dense depth. As can be seen in Fig. 1, they form fundamental input for the warping operation which we will describe in the following.

The radar RD grid is given by coordinates of radial relative velocity v_r and range $|\mathbf{x}_r|$ seen from the radar perspective. These can be obtained as described in Eq. 1a-1f, 15, 18 for every pixel in the camera image. In our warping operation $\eta(\cdot, \cdot) : \mathbb{C}^2 \rightarrow \mathbb{C}^2$, we select for each pixel in the camera image the corresponding pixel in the RD grid depending on the assigned $v_r(\boldsymbol{\xi})$ and $|\mathbf{x}_r|$ and project the assigned RD grid pixel value back into the camera image grid. Since $v_r(\boldsymbol{\xi})$ and $|\mathbf{x}_r|$ do not automatically align with the RD grid, we select bi-linear interpolation, as it provides visually appealing projections, while still being differentiable and therefore rendering NN training possible.

The warping operation is illustrated in Fig. 7 for warping of the RD-map into the camera image and thus helping a developer to understand how a radar sees environment in terms of power in a human understandable fashion. We will refer to the projected RD-map as \mathcal{RD}_C further on.

\mathcal{RD}_C can be calculated at the pixel position $\{u, v\}$ as:

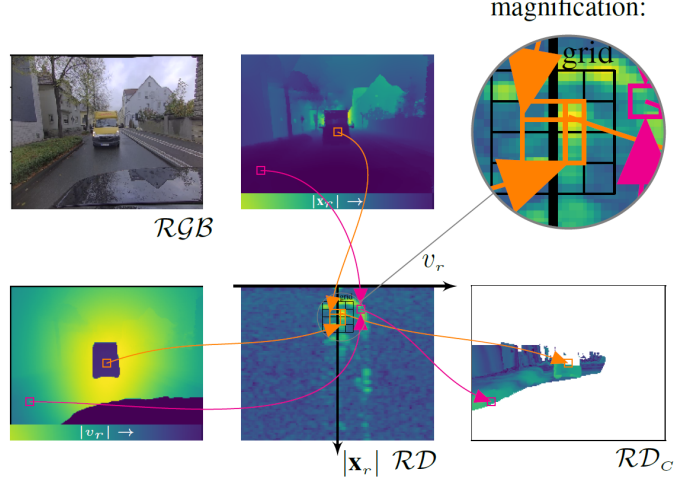


Figure 7. **RD-map warping into camera image:** As an example for the warping operation, here for two pixels in the camera image (upper left) their estimated range (upper center) and radial velocity (lower left) determines their corresponding position in the RD-map (lower center). The RD-map's intensity value is bi-linear interpolated (upper right) and then projected into the camera image (lower right). Notice that only power from radar FoV is warped here (\mathcal{RD}_C)

$$\mathcal{RD}_C(u, v) = \eta \left(\mathcal{RD}(\mathbf{p}_s^{ij}); v_r(\boldsymbol{\xi}), |\mathbf{x}_r| \right) = \sum_{i,j \in \{-0.5, 0.5\}} w^{ij} \mathcal{RD}(\mathbf{p}_s^{ij}), \quad (22a)$$

$$\mathbf{p}_s^{ij} = \left\{ [v_r(u, v) + i]_{\Delta v}, [r(u, v) + j]_{\Delta r} \right\}, \quad (22b)$$

thus \mathbf{p}_s^{ij} being one of four corners of a pixel in the RD grid, corresponding to the camera image pixel $\{u, v\}$. The weight w^{ij} is linear proportional to the spatial proximity in RD grid and $\sum_{i,j} w^{ij} = 1$, similar to [44]. Differentiability of bi-linear interpolation has already been proven in e.g. [45] and is mandatory property for the underlying work, as it allows error backpropagation through the warping operation, into the NN and thus enables network training. Note, that in Eq. 23c and Fig. 7 the RD-map \mathcal{RD} was depicted as an illustrative example for the warping operation. However, every information in the form of the RD grid can be warped into a camera image analogously. In fact, we will warp a radar based prediction by NNs analogously in the upcoming section as depicted in Fig. 1.

VI. CROSS-MODAL SUPERVISED LEARNING ON RADAR SPECTRUM DATA

While leveraging camera based label predictions for other sensors already exists, see e.g. [46], to the best of our knowledge, this is the first work to apply “teacher-student design” between camera and radar spectrum.

In this section, we describe the generic handling of warping errors between camera and radar to achieve a better training of the student networks. Then, explain implementation details of the used convolutional neural networks (CNNs) for the radar based DoA estimation as well, as the label generation and train objective.

A. Novel automatic warping error handling via loss scale-space

Even though our DRISFWR approach is able to align the estimated scene flow with respect to the radars RD-map, warping from radar spectrum to camera image can be incorrect when there is an error in $v_r(\xi)$ and $|\mathbf{x}_r|$ exceeds the resolution of the radar. As a consequence, it leads to performance degradation in CNN training. To mitigate this effect, we create image pyramids by subsampling the NNs prediction and thus virtually reducing the radars RD resolution depending on scale-level s . Here $S = 3$ scale-levels were used.

Subsampling is performed via 2D-average pooling on prediction in RD grid, weighted by RD bin power. Hereafter, the prediction on every scale space level is warped into a camera image and compared to the corresponding camera label to create a per scale loss, which is summed up in the training objective, see Fig. 8. The effective RD resolution is bisected at each scale-level.

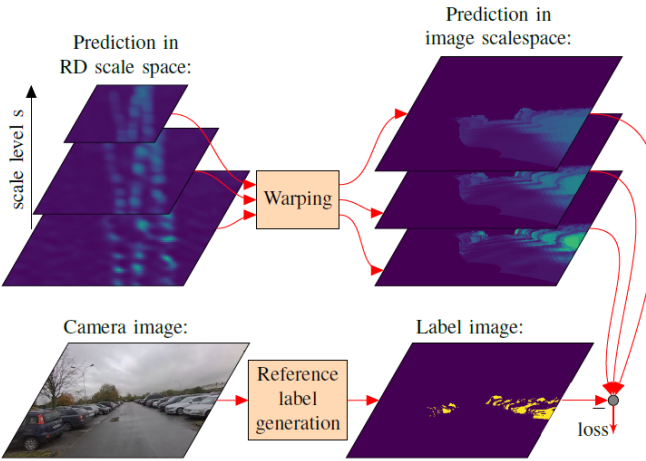


Figure 8. **Loss in scale-space:** As accurate warping operations require an accuracy better than the RD resolution, we downscale RD grid to virtually reduce the later resolution and thus mitigate warping errors to forestall the training process.

B. Radar based DoA prediction via Neural Network

To estimate the DoA of the radar reflections, a CNN architecture is used to operate on the radar spectra \mathcal{U} . To be precise, the radar spectra of the utilized 3 channel radar $\{\mathcal{U}_1, \mathcal{U}_2, \mathcal{U}_3\}$ with non uniform spacing antennas is preprocessed before being transferred to the network. The first feature map is the RD-map, while the second and third feature maps are the phase spectra $\angle(\mathcal{U}_i, \mathcal{U}_{i-1})$ between adjacent channels by multiplying the complex signal \mathcal{U}_i with the normalized, conjugated signal from adjacent antenna:

$$\Gamma = \begin{bmatrix} \mathcal{RD} \\ \angle(\mathcal{U}_2, \mathcal{U}_1) \\ \angle(\mathcal{U}_3, \mathcal{U}_2) \end{bmatrix} \quad (23a)$$

$$\angle(\mathcal{U}_i, \mathcal{U}_{i-1}) = \arctan 2(\Re\{z_i\}, \Im\{z_i\}) \quad (23b)$$

$$z_i = \mathcal{U}_i \frac{\mathcal{U}_{i-1}^*}{|\mathcal{U}_{i-1}|} \quad (23c)$$

For every pixel in the RD grid, the NN provides a single DoA estimation $\phi_{\text{RD-grid}}$ in azimuth direction which is warped into a camera image as $\phi_{\text{predict, RD-grid}}$:

$$\phi_{\text{predict, RD-grid}} = \phi\text{-Net}(\Gamma) \quad (24)$$

$$\phi_{\text{predict, cam}} = \eta(\phi_{\text{predict, RD-grid}}; v_r(\xi), |\mathbf{x}_r|). \quad (25)$$

DoA labels $\phi_{\text{reference}}$ are generated from the dense-depth estimation in the camera image projected into radar-COOS as:

$$\phi_{\text{reference}} = \arctan 2(x_{R,x}, x_{R,y}). \quad (26)$$

Predictions of ϕ -Net are made, so that the objective $l_{\phi\text{-Net}}$ is minimized during network training:

$$l_{\phi\text{-Net}} = \sum_{\mathbf{p} \in P_{\text{radar}}} \sum_{s \leq S} \frac{1}{s} |\phi_{\text{reference}}(\mathbf{p}) - \phi_{\text{predict, cam}}(\mathbf{p})|, \quad (27)$$

in which summation is done over all pixels \mathbf{p} , in the radars FoV and positive RD-map power, as we want the network to focus on relevant targets. Furthermore, loss is formed over all scales (see Sec. VI-A) with reciprocal contribution. Examples for $\phi_{\text{reference}}$, $\phi_{\text{predict, cam}}$ and $\phi_{\text{predict, RD-grid}}$ are depicted in Fig. 11.

The selected CNN architecture has ReLU activations on every layer except the last, where $90 \cdot \tanh()$ is applied to scale the logits angular values in degree. The convolutions are operated with unit stride and follows channel count $[3, 32t, 64t, 128t, 64t, 32t, 32t, 1]$ from input to output. We tested three different architectures, with convolution kernel size of 1×1 and 3×3 . The inference of the former one will be influenced by one pixel in the RD grid only, while the later one may use a RD grid pixel vicinity to perform inference. The receptive fields thus compute to 1 ($0.25 \text{ m} \times 0.25 \text{ m s}^{-1}$) and 15 ($3.75 \text{ m} \times 3.75 \text{ m s}^{-1}$) respectively. To test the influence of parameter count, we modify the layer numbers via t . The parameters of the three tested NN architectures are depicted in Tab. I.

Name	kernel size	layer modifier (t)	parameter count
NN (1x1)	1×1	1	$\approx 22k$
NN (1x1 ext.)	1×1	9	$\approx 1745k$
NN (3x3)	3×3	1	$\approx 195k$

Table I
NN ARCHITECTURES. PARAMETERS OF THE UTILIZED NN ARCHITECTURES

C. Training dataset and optimizer

Before the training, we split our 1 h long dataset (Fig. 2) into 10 s long sequences a 100 frames. The sequences are randomly assigned to train, evaluation and test data 70%, 15%, 15% with no frame overlap thus creating partially statistically independent samples.

All networks are optimized via ADAM and a learning rate of 10^{-5} on training data. Early stopping was performed by checking network performance on evaluation dataset after each training epoch.

VII. EVALUATION

A. Scene flow evaluation

To benchmark the performance of our proposed scene flow algorithm, it was necessary to create a new dataset which contains data from lidar, DGPS-INS, camera and radar RD-maps and ground truth reference for scene flow. We choose to benchmark the algorithms in parking space scenarios (see Fig. 2) with all objects being stationary, in which precise ego-motion from the DGPS-INS and ground-truth motion in form of relative motion to the objects is known. This approach is feasible, since stationariness is not enforced for the algorithms and thus neither has an advantage over the other. For a more elaborate scene flow ground truth generation technique, the reader is referred to KITTI datasets approach [47]. However, for stationary scenes, both approaches are identical and thus we select our approach for simplicity only. Scene flow in stationary scenes has been described in Sec. IV-C and thus scene flow ground truth ξ_{gt} is calculated by $\xi_{gt} = \xi_{bg}$.

The KITTI dataset provides scene flow evaluation metrics mainly in camera image plane direction. Here, scene flow errors orthogonal and tangential to the image plane are important and thus we decided to use error metrics considering normal and tangential errors equally. The first evaluations metric is the mean absolute error

$$\text{MAE}_{sf} = \frac{1}{N} \sum_{\mathbf{p}_{sf} \in P_{sf}} \|\xi_{gt}(\mathbf{p}_{sf}) - \xi(\mathbf{p}_{sf})\|_2^1 \quad (28)$$

$$P_{sf} := \{\mathbf{p} \mid \mathbf{p} \in P_{\text{radar}} \wedge \mathbf{p} \in P_{\text{sparse}} \wedge \mathbf{p} \in P_{\text{fg}}\},$$

of ground truth and estimated scene flow for all pixels \mathbf{p} visible to the radar, have assigned lidar sparse depth measurement and instance mask (foreground pixels). N is the quantity of pixels that coincide with the conditions.

The second evaluation metric is the scene flow error rate, which is the number of foreground pixels exceeding an error threshold of 0.25 m/s , which is a typical radar velocity resolution.

As can be seen in Tab. II the DRISFwR algorithm achieves better metrics than the current top-ranking scene flow estimation algorithm in KITTI benchmarks. Both algorithms assign strong motion prior, by assuming rigid bodies for each instance from instance segmentation. As an alternative scene flow estimation technique with weak motion constraints, we include an estimation based on optical flow by warping depth images between frames via HD³ [37]. It can be seen, that scene flow performance without strong motion prior assumption does not stand a chance. Which we found reasonable, as the nominal accuracy of the reference system is 0.16° tangential and 0.03 m radial giving a theoretical three-dimensional accuracy of $\approx 1.42 \text{ m s}^{-1}$ for a target in 20 m distance. Rigid object assumption often results in hundreds of pixel level samples per object allowing to under exceed the nominal accuracy of the reference sensors itself.

Note, that for our application the effective error is likely smaller than the provided values, as we only require accurate radial velocity estimate, whereas in the metric, we also punish tangential velocity deviations.

Methods	runtime	error rate (%)	MAE (m/s)
HD ³	0.12 sec	69.9	4.37
DRISF [35]	0.6 sec	31.2	0.31
DRISFwR	0.8 sec	25.5	0.22

Table II
QUANTITATIVE COMPARISON TO OTHER SCENE FLOW APPROACHES.
DRISFwR REDUCES SCENE FLOW DEVIATIONS AND ERROR RATE COMPARED TO DRISF AND THE MOSTLY PRIOR FREE ESTIMATOR HD³.

Supporting results and investigations can be found in Appendix A.

B. Direction of Arrival evaluation

DRISFwR helps to warp radar spectrum to camera images without human supervision, within the scope of the evaluated accuracy, see prior section. However, sometimes scene flow is found to be erroneous, so that

- stationary objects are mis-labeled as moving
- significant portions of the RD-map power is not transferred into \mathcal{RD}_C .

Fortunately, these types of errors can easily be spotted by a trained human and labeled as anomalies and thus be excluded from the subsequent comparison between the reference data and the estimates from radar. Thus, with the help of our reference label generation system, the labeling task has been tremendously simplified from a regression problem (draw DoA reference angles) to a binary classification problem (identify whether proposed label seems plausible or not) for the human labeler. Our test dataset (10800 images) has been labeled following this process. Examples of the anomaly masks are illustrated in Fig. 9. From all test images, approx. 20.3% received at least one anomaly mask. The average labeling time per image was approx. 5 s. The NN training however, was performed without human intervention.

Typically the radar based estimation is highly influenced by the underlying signal-to-noise-ratio (SNR) and thus is often plotted to each other. Here, signal is estimated as the power value of the corresponding pixel in the RD-map. The noise estimate is generated as the 99.5% percentile of all CFAR classified non-target pixels in the RD-map [40]. $\mu + 3\sigma$ value of identified clutter in the RD-map. In stationary scenes with low ego-vehicle velocity $< 2 \text{ m s}^{-1}$, the signal power from multiple reflections accumulates in the zero Doppler velocity pixels. These signal powers cannot be recovered, leading to erroneous signal power estimation. Stationary scenes are thus discarded from the test dataset.

The warping operation is non-bijective in the sense that multiple pixels in the camera may correspond to a single pixel in the RD-map and vice-versa. In evaluation this typically means (as the former case is more typical), that one estimation value (one pixel in the RD grid) is compared to an ensemble of reference values \mathcal{P}_s (multiple pixels in the camera image). Ideally, one would want to assign an electromagnetic contribution of each reference pixel and compute the center of reflection to which the estimation value is then compared to. However, at the current stage of this reference system, the electromagnetic contribution remains latent. In practice, we

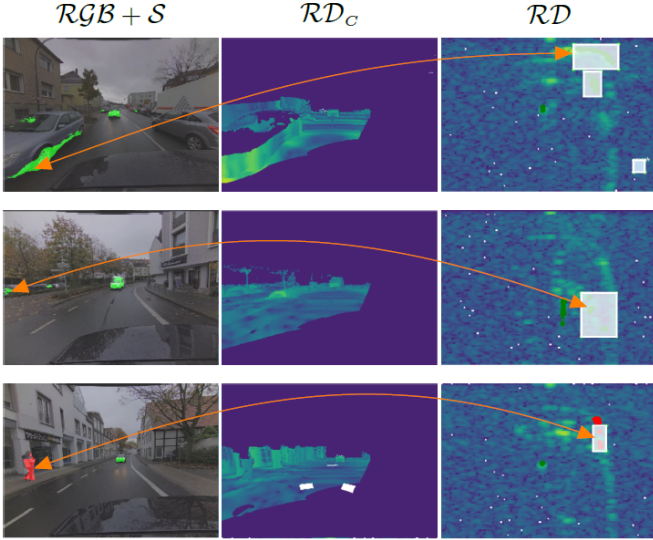


Figure 9. **Examples of anomaly labels:** From left to right: camera images with semantic instance masks from radar FoV only (red: pedestrian, green: vehicle), projected RD-maps, RD-maps with semantic masks and anomaly masks (white rectangles). The orange arrows draw region correspondence between camera image and RD-map. In the two upper rows, stationary objects were labeled as moving, due to error in scene flow estimation. However, the misalignment in RD-map is subjectively small. The lower row example indicate error in instance segmentation, in which background pixels were mapped as pedestrian, resulting in extended object range in RD-map.

select the best matching pixel from the camera ensemble to the RD grid pixel as the tuple $\{\mathbf{p}_C, \mathbf{p}_{RD}\}$ such that

$$\mathbf{p}_{RD}(\mathbf{p}_C) = \arg \min_{\mathbf{p}_s \in \mathcal{P}_s} \left| \phi_{\text{reference}}(\mathbf{p}_C) - \eta \left(\phi_{\text{predict, RD-grid}}(\mathbf{p}_s); \xi, \mathbf{x}_r \right) \right|. \quad (29)$$

The DoA MAE metric is thus computed as

$$\text{MAE}_{\text{DoA}} = \frac{1}{N} \sum_{\mathbf{p}_C \in \mathcal{P}_{\text{radar}}} \left| \phi_{\text{reference}}(\mathbf{p}_C) - \phi_{\text{predict, RD-grid}}(\mathbf{p}_{RD}(\mathbf{p}_C)) \right|, \quad (30)$$

where N is the number of RD grid pixels visible to camera and radar. The MAE metric is calculated for different DoA estimators similarly and depicted in Fig. 10.

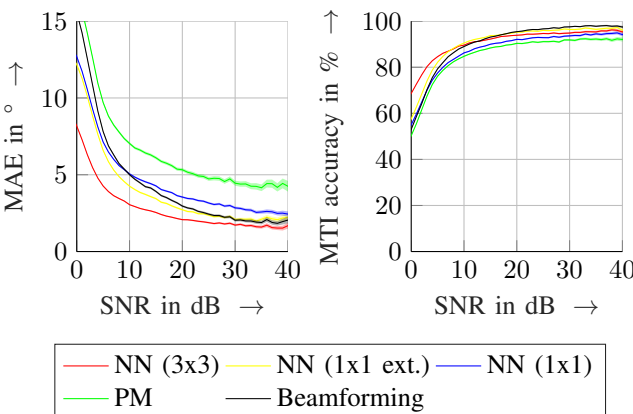


Figure 10. **Comparison of DoA estimation methods:** Mean Absolute Error of estimation vs. reference and mean error over azimuth angle. CNN with kernel-size 3 (red), phase-monopulse (green), CNN with kernel-size 1 (blue and yellow) and beamforming (black).

We include the phase-monopulse (PM) DoA estimator and Bartlett beamforming as baseline non-supervised type algorithms. It can be seen, that the (3x3) and (1x1 ext.) NN estimators achieved significantly lower MAE over the entire SNR range. Furthermore, the DoA estimator with an increased receptive field in the RD-grid outperforms similar estimators performing inference on a single RD-grid pixel only. This suggests, that neighboring RD-map pixels carry statistical dependencies which can be used for a better DoA inference. We explain the statistical dependencies by (a) windowing performed before computing the FFT based RD grid and whereby energy is smeared over multiple pixels and (b) geometrically neighbouring pixels in cartesian coordinates (or camera) share similar locations in the RD-grid.

Additionally, we perform DoA evaluation via moving target indication (MTI), which heavily relies on DoA predictions to classify stationary and moving targets. The utilized MTI algorithm can be found in [48], [49]. We set reference labels for moving pixels when $\|\xi_{fg}\|_2^2 > 0.5 \text{ m s}^{-1}$ and stationary otherwise. MTI accuracy is calculated by comparing the prediction to the reference label in similar fashion as above.

In the MTI evaluation plot, the difference between the DoA estimators repeat to display. In low SNR regions, the (3x3) NN achieved better accuracy compared to the other estimator, although surpassed at higher SNRs.

Qualitative examples are depicted in Fig. 11 for the DoA labels and predictions. It can be seen, that the color hue between DoA label and DoA prediction images mostly match and thus the predictions mostly resemble the DoA labels. The main difference between DoA label and prediction images comes from the selected visualization method, in which the color intensity of the prediction is scaled by the underlying RD-map SNR value. This visualization method helps to focus on regions with high SNR values and suppresses the cognition of low SNR values e.g. irrelevant noise regions. Comparing the grayscaled DoA prediction of the NN to the PM predictions in RD-grid, the PM prediction appear to be statistically independent, especially in the low SNR regions.

C. Other applications

The proposed framework has also been tested in the applications of target detection, semantic segmentation and power estimation from camera. Our observations and qualitative results can be found in Appendix B, C and D.

VIII. CONCLUSION

In this paper we developed an algorithm for warping FMCW radar data into camera image, enabling us to utilize high-quality labels generated from camera and lidar reference sensors. Large CNNs for DoA inference were trained on these labels and achieve qualitative and quantitative equal or better performance than classical baseline radar processing algorithms. Furthermore, beneficial influence of utilizing pixel vicinity when performing DoA inference was shown with the help of different NN receptive fields. Although the general approach of utilizing pixel vicinity for better estimation is known from e.g. classical image processing, to the best of

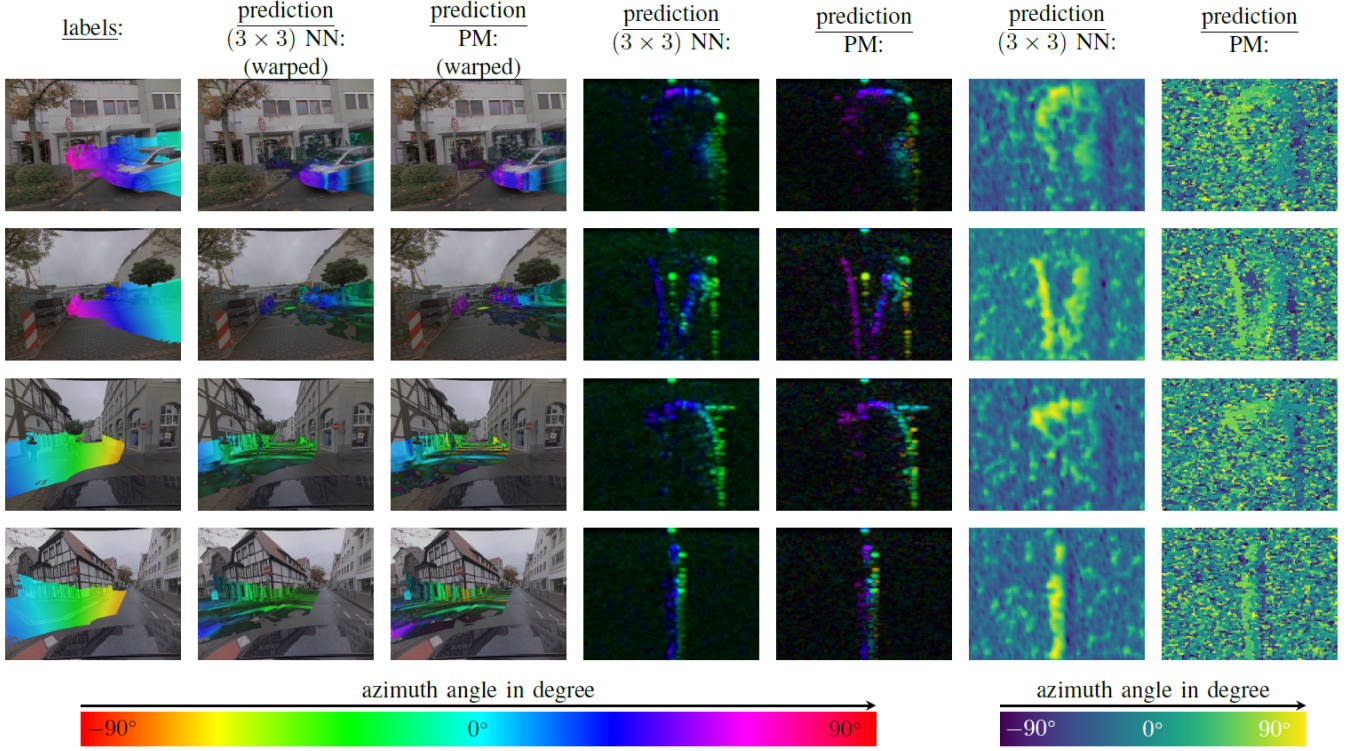


Figure 11. **Qualitative results of Direction-of-Arrival estimation on test data examples.** From left-to-right: RGB image with color coded azimuth labels, RGB image with color coded azimuth predictions from NN, RGB image with color coded azimuth predictions from PM, RD-map with color coded azimuth prediction from NN, RD-map with color coded azimuth prediction from PM, azimuth predictions from NN in RD-grid, azimuth predictions from PM in RD-grid.

our knowledge, we are the first to utilize this in radar based DoA inference. The development of this automatic labeling approach was key for this observation, as it enabled us to gather densely labeled and high-resolution frequency-level radar data from real world driving scenarios with extended radar targets (geometrically and kinematically).

The framework has also been tested in the applications of target detection, semantic segmentation and SNR estimation from camera. In all applications the trained NN were able to achieve reasonable predictions, even though label noise was identified as e.g. warping errors and erroneous aspect-angle estimation. As the warping operation projects the frequency-level radar data and NN predictions into camera image, the results are easy to understand for humans and allow qualitative assessment.

The foundation to the warping was the development of a novel scene flow estimation algorithm utilizing radar, camera and lidar data.

APPENDIX A

FURTHER EVALUATION OF DRISFwR

To support the scene flow evaluation from Sec. VII-A, we provide qualitative comparison of the three compared scene flow algorithms in Fig. 12.

It can be seen, that in all examples DRISFwR provides better results than DRISF and especially as the scene flow algorithms without strong motion priors.

In Sec. IV-C we mentioned slightly observed inaccuracy in reference scene flow based on DGPS-INS motion and the

motion refinement via camera. To investigate for remaining systematic scene flow error, the scene flow error between the reference scene flow and the scene flow estimations based on DRISF and DRISFwR are plotted in Fig. 13 against the ego-vehicles rotational motion (yaw rate). It can be seen, that the scene flow errors are nearly constant. Even though not presented here, a significant drift in scene flow error without the camera motion refinement was observed. As the scene flow error drifts only marginal over yaw rate, we conclude, that the reference scene flow was calculated reasonable.

APPENDIX B TARGET DETECTION VIA NEURAL NETWORK

As another classical radar signal processing application, beside DoA estimation, target detection can be performed via NN. Compared to DoA, we found that automatic label generation is significantly more challenging for target detection as it is for DoA. For the DoA application, the reference sensor system provides direct resolution in the label units (via Eq. 2a-2c) and thus the labels can be seen as ground truth. However, for target detection the the reference labels must be estimated as the reference system has no native understanding of what the radar sensor sees and what not. Our label estimation approach for target detection is arguable, but we still wanted to share our current research to others and therefore we decided to include this section into appendix rather than the main section of this paper.

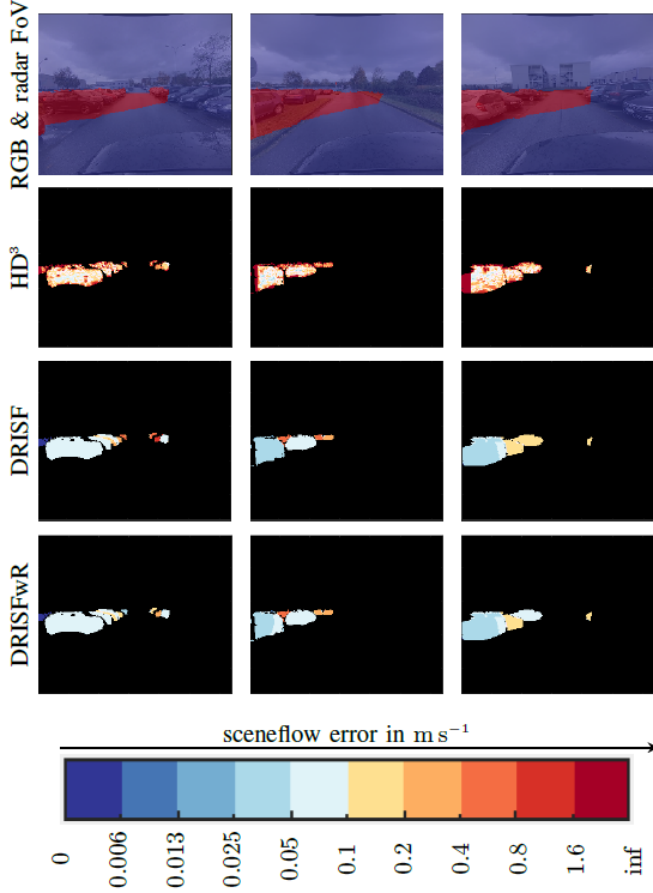


Figure 12. **Qualitative results of scene flow algorithms on test data examples:** From top-to-bottom: radar FoV coverage within RGB image, scene flow error of HD³, scene flow error of DRISF, scene flow error of DRISFwR. Our method was able to achieve lower object scene flow errors in general. Notice, that only foreground objects in radar FoV are taken into account for evaluation, thus remaining pixels are colored black.

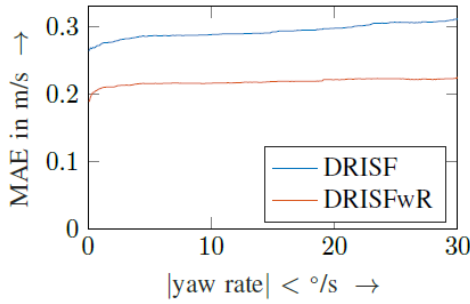


Figure 13. **Motion analysis.** Cumulative distribution function of scene flow error versus yaw-rate. On average DRISFwR reduces scene flow deviation even when ego-vehicle is cornering.

A. Label generation

The neural network (TD – Net) is trained against virtual reflectors Ω_{GT} from reference system, which are deduced based on geometric properties of the reflecting objects in the dense depth map. From literature, e.g. [50], [52], it is well known, that radar reflectivity highly depends on the aspect angle between radar on reflector surface. We calculate the aspect angle with the cosine similarity via scalar projection

as follows,

$$\cos(\angle(\mathbf{x}_R, \mathbf{n}_R)) = \frac{\mathbf{x}_R \cdot \mathbf{n}_R}{\|\mathbf{x}_R\| \|\mathbf{n}_R\|}, \quad (31)$$

where \mathbf{x}_R is the ray direction and \mathbf{n}_R is the surface normal from dense depth seen from radar perspective. Surface normal is calculated from \mathbf{x}_R , by taking cross product of quadrilaterals in image plane. The entity of cosine similarity for all pixels is consolidated in \mathcal{A} .

As the TD – Net training requires one-hot encoded labels, we seed virtual target label in camera image, when the cosine similarity value exceeds $|\cos(\angle(\mathbf{x}_R, \mathbf{n}_R))| \geq 0.5$. This value is inspired by Rayleigh criterion [53] describing surface smoothness related to wavelength and by empirical investigation. Further physical modeling of reflectivity based on electromagnetic properties is not carried out and postponed for future investigations.

B. Network architecture

TD – Net has similar architecture as ϕ – Net, except for last layer being single output with sigmoid activation to model per-pixel confidence Ω of significant reflection. Input data for the network is the RD-map from radar spectra.

C. Optimization

For network optimization binary cross entropy is utilized as cost function,

$$l_{\text{TD-Net}} = - \sum_{\mathcal{P}_{\text{radar}}} \sum_{s \leq S} \frac{1}{s} \left(\Omega_{\text{GT}} \log(\Omega) + (1 - \Omega_{\text{GT}}) \log(1 - \Omega) \right). \quad (32)$$

D. Results

Qualitative results are visualized in Fig. 14 for the reference labels, the neural network predictions and a classical CFAR estimation as reference.

It can be seen, that the color distribution between the reference mask and the predicted mask in camera image mostly match. One major difference between the NN based prediction and the CFAR prediction is that the later one does only categorical prediction (either target or no-target). Apart from that, the authors did not find major difference between NN based target detection and CFAR based target detection.

As declared, the reference labels for target detection highly depend on the utilized vision model and therefore we disclaim to provide quantitative results.

APPENDIX C SEMANTIC SEGMENTATION VIA NEURAL NETWORK

Another application for our proposed pipeline is the semantic segmentation of RD-spectrum data. Each pixel in RD grid is classified as being stationary (against the world), moving pedestrian, moving vehicle or background.

In [48], [49] we proposed a hypothesis test for the detection of moving radar targets based on their relative radial velocity and DoA measured by a radar.

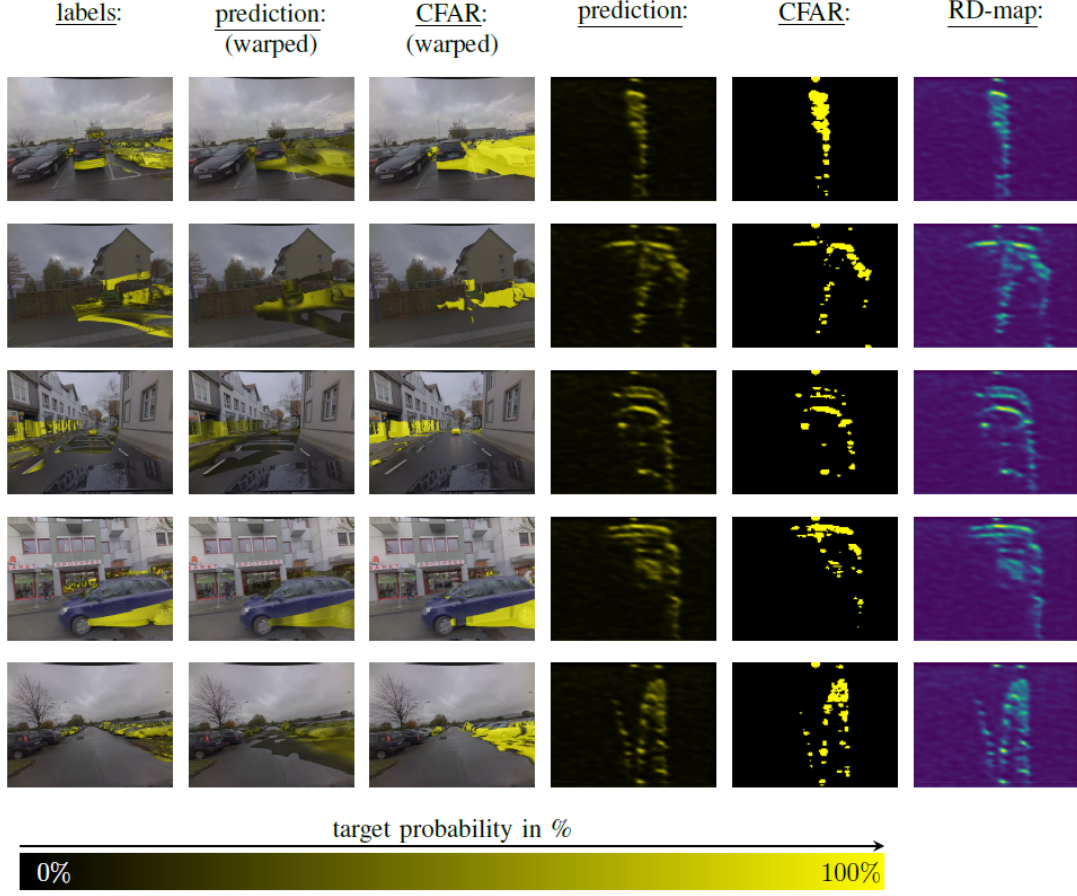


Figure 14. **Qualitative results of target detection on test data examples.** From left-to-right: RGB image with color coded target labels, RGB image with color coded target predictions from NN, RGB image with color coded target predictions from CFAR, RD-map with color coded target prediction from NN, RD-map with color coded target prediction from CFAR, RD-map.

This hypothesis test is simple, yet very accurate, thus we decide to inherit it into the classification network in modified form. The modified and differentiable version of the hypothesis test is given as

$$\Pr(p == c_{\text{moving}}) = \exp \left\{ \frac{\mu_E^2}{(\sigma_E \cdot Q^{-1}(\alpha/2))^2} \right\}, \quad (33)$$

were μ_E and σ_E are the difference in between measured radial relative velocity and expected velocity for stationary targets and expected velocity variance. $Q^{-1}(\alpha/2)$ is the inverted (Gaussian) tail distribution function under the level of significance α . Gaussian activation function was used, motivated by the modeling of μ_E as being Gaussian distributed (and producing sharper decisions compared to Softstep-function). With this, instead of being categorical $\Pr(p == c_{\text{moving}})$ now converts into a continuous variable $\in [0, 1]$, which increases for stationary targets/objects and decreases for moving objects. The value is computed on pixel level in the RD-map (\mathcal{MT}) and warped into camera image (\mathcal{MT}_C) with one scene example illustrated in Fig. 15.

A. Network architecture

The NN architecture (Ψ -Net) is similar to ϕ -NN, except that at first layer, the 3D radar spectra and the output of

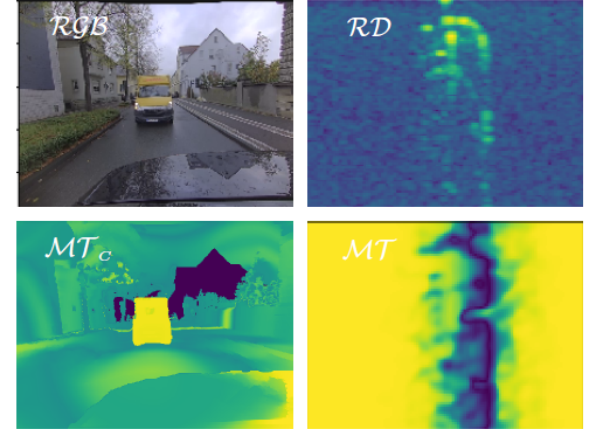


Figure 15. **Example of moving type indication.** Top-row: RGB image, RD-map; Bottom-row: Moving target confidence (brighter values mean higher confidence) estimated by neural network in camera image and in RD-map. The ego-vehicle was moving with the postal truck following.

stationary target detection step are convolved individually and the outcome is concatenate towards the second layer. The output channel size is also increased to 3 to provide multi-label confidence.

B. Optimization

For training of Ψ -Net, focal-loss [54] was evaluated between semantic segmentation prediction on RD-map projected into camera image Ψ and the semantic segmentation from teacher network Ψ_{GT} native in camera image. The class predictions of Ψ -Net are {“stationary”, “pedestrian”, “vehicle”, “background”} which express if a RD-map pixel stationary or a moving pedestrian or vehicle. The focal-loss cost function is utilized with cost scaling $w_c = [1, 500, 10]$ to mitigate class-imbalance and empirically found to achieve better classification,

$$l_{\Psi-\text{NN}} = - \sum_{\mathcal{P}_{\text{radar}}} \sum_{s \leq S} \frac{1}{s} \left(w_c (1 - \Psi)^2 \Psi_{\text{GT}} \log(\Psi) + \Psi^2 (1 - \Psi_{\text{GT}}) \log(1 - \Psi) \right). \quad (34)$$

Label for “stationary” is set high, if semantic segmentation classifies pixel as pedestrian or vehicle, its DRISFwR scene flow deviates from stationary scene flow (see IV-C) only marginal in its radial component (0.6 m s^{-1}) and if Ω_{GT} is true. Remaining labels for “pedestrian” and “vehicle” come from semantic segmentation on RGB image.

C. Results

Qualitative results are visualized in Fig. 16. It can be observed, that the color of the semantic mask predicted by the neural network and warped into camera image mostly resembles the reference label mask and that the predictions are reasonable. The authors found, that the main difference between the predicted semantic mask and the reference mask occurs in different distributions of intensity in the images. This can be explained, as the reference masks intensity is based on aspect angle, while the NN learned to create mask intensity based on SNR value in the RD-map. One example of this can be seen by comparing the reference labels and the predictions of the third example in Fig. 16. The reference labels of the parking car, shown left in the images, are significantly noisy whilst the predictions occur reasonable. The fact that the Ψ -Net was still able to estimate reasonable semantic masks in real world scenes suggests, that (a) utilizing aspect angle to estimate reference masks is appropriate and (b) the presented algorithms for robust NN training (scalespace costs and optimization criteria) in conjunction with large amounts of training data helped to train the NN despite significant label noise. Due to significant label noise, we disclaim to provide quantitative results.

APPENDIX D

ESTIMATING RADAR SNR FROM CAMERA

The main contribution of this paper was the design of a teacher-trainer framework for radar based NN training against labels from camera vision models. However, with minor modifications to the framework, see Fig. 17, it is also possible to train camera fed estimators against radar data.

As an example of this approach we train a NN to estimate the radars RD-map SNR values from camera input. Therefore,

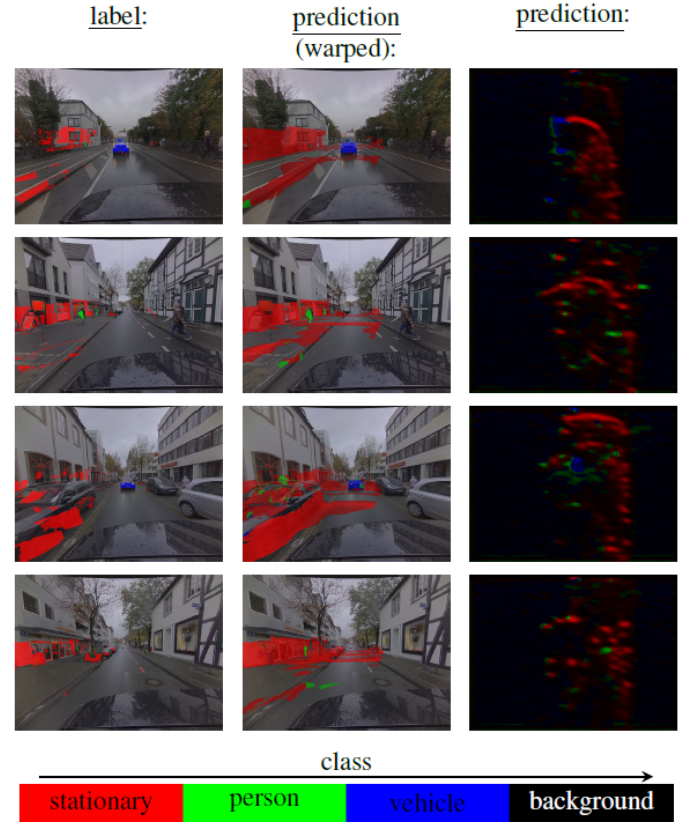


Figure 16. **Qualitative results of semantic segmentation on test data examples.** From left-to-right: RGB image with color coded semantic mask labels, RGB image with color coded semantic predictions from NN, RD-map with color coded semantic predictions.

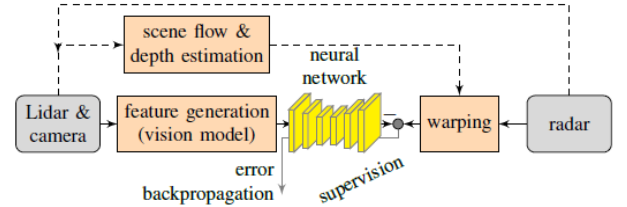


Figure 17. **Overview of the model pipeline for camera based estimators:** Utilization of the reference sensors (lidar & camera) and the radar for the supervised training of a neural-network operating on camera data.

we use the notation SNR-NN to describe this specific network. We found this approach useful as it might be helpful for the development of e.g. radar raytracing software.

A. Network input feature maps

As inputs for the SNR-NN, the dense depth map, semantic mask, aspect angle image and the camera RGB image are provided. The depth map is provided, as range is an important power modulation factor in radar range equation [40]. Semantic mask is used, as by physic radar-cross-section (RCS) and thus SNR highly depends on material characteristics. The idea was, that once the NN knows class properties, it can generate a intrinsic guess of material properties used in different traffic participants. Aspect angle image was used, to provide the NN a

prefabricated idea on how much emitted power from the radar is redirected back to the radar as reflection or transmission into space. Additionally the raw rgb image is provided, to allow the NN to extract visual cues itself, which are not covered by the pre-processed image features.

B. Network architecture

The DNN architecture is fully convolutional with ReLU activations on every layer. The convolutions are 3×3 with unit stride and following channel count [16, 32, 64, 32, 16, 16, 1]. The input feature maps are reprocessed via single layer convolution separately, where each feature map results in 4 intermediate channels. Intermediate channels from feature maps are then concatenated as input for the neural network.

C. Optimization

Assuming Swerling type 3 fluctuations (see e.g. [50]) in the reflected radar echo, we can model the observed RCS σ as a Chi-squared distribution from the true RCS $\bar{\sigma}$

$$p(\sigma|\bar{\sigma}) = \frac{4\sigma}{\bar{\sigma}^2} e^{-2\frac{\sigma}{\bar{\sigma}}}. \quad (35)$$

Hence the received signal power linear scales with the RCS (see radar range equation), we obtain loss function for the neural network by calculation of the maximum-likelihood (ML) estimator for $\bar{\sigma}$ via derivative of log-likelihood functions

$$\log(L(p)) = \log \left(\prod_i \frac{4\sigma}{\bar{\sigma}^2} e^{-2\frac{\sigma_i}{\bar{\sigma}}} \right) \quad (36)$$

as

$$\frac{\partial \log(L(p))}{\partial \bar{\sigma}} = \sum_i^N (\sigma_i - \bar{\sigma}) \quad (37)$$

and

$$\bar{\sigma}^{(ML)} = \frac{\sum \sigma_i}{N}. \quad (38)$$

From Eq. 37 we see, that in order to optimize SNR estimate, we need to minimize the difference between radar measured SNR \mathcal{RD}_C (warped power spectra from radar) and estimated SNR $\mathcal{RD}_{\text{prediction}}$ (estimated power from SNR-NN). Which results in the utilized loss function as

$$l_{\text{SNR-NN}} = \sum_{\mathcal{P}_{\text{radar}}} \sum_{s \leq S} \frac{1}{s} |\mathcal{RD}_{\text{prediction}} - \mathcal{RD}_C|. \quad (39)$$

As convexity is required for minimization via gradient descent, the sign of the difference is omitted by introducing the value function.

D. Results

The SNR-NN neural network is optimized on our dataset as described before. Qualitative results can be found in Fig. 18. By closer inspection, artefacts present in the aspect angle maps (mostly in regions depth was mostly sparse from lidar scanner) can be relocated in the estimated SNR maps $\mathcal{RD}_{\text{prediction}}$. We conclude, that the NN learned dependencies between the aspect angle feature map from reference sensors and the radar received power. A significant portion in the \mathcal{RD}_C images is suppressed (dark blue area), as it is not covered by the radars FoV, whilst the NN is designed to generalize the same regions in $\mathcal{RD}_{\text{prediction}}$.

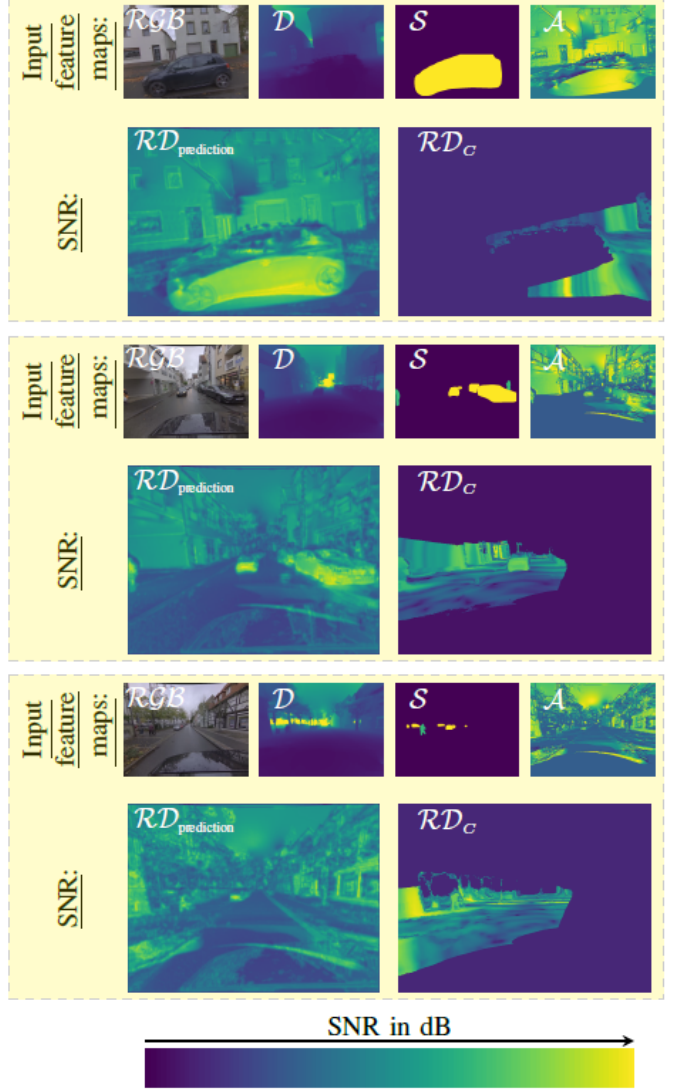


Figure 18. **Qualitative results of SNR prediction on test data.** Each yellow block corresponds to one sample frame. In the block, the upper row visualizes the feature maps for the neural network (rgb image, depth image, semantic mask, aspect angle image). The lower rows show the predicted SNR by the neural network and the warped SNR (only pixels from radar FoV) from radar spectra against which the neural network is trained.

REFERENCES

- [1] J. Heymann, L. Drude, R. Haeb-Umbach, K. Kinoshita, and T. Nakatani, “Joint optimization of neural network-based WPE dereverberation and acoustic model for robust online ASR,” in *IEEE International Conference on Acoustics, Speech and Signal Processing, ICASSP 2019, Brighton, United Kingdom, May 12-17, 2019*. IEEE, 2019, pp. 6655-6659. [Online]. Available: <https://doi.org/10.1109/ICASSP.2019.8683294>
- [2] D. Ciresan, U. Meier, J. Masci, and J. Schmidhuber, “Multi-column deep neural network for traffic sign classification,” in *Proceedings of the International Joint Conference on Neural Networks (IJCNN)*, 2011.
- [3] X. Zhu, D. Tuia, L. Mou, G. Xia, L. Zhang, F. Xu, and F. Fraundorfer, “Deep learning in remote sensing: A comprehensive review and list of resources,” *IEEE Geoscience and Remote Sensing Magazine*, vol. 5, 2017.
- [4] A. Geiger, P. Lenz, C. Stiller, and R. Urtasun, *Vision meets Robotics: The KITTI Dataset*. International Journal of Robotics Research (IJRR), 2012.
- [5] A. Geiger, P. Lenz, and R. Urtasun, “Are we ready for autonomous

driving? the kitti vision benchmark suite,” in *Proceedings of the IEEE Conference on Computer Vision and Pattern Recognition (CVPR, 2012)*.

[6] M. Menze and A. Geiger, “Object scene flow for autonomous vehicles,” in *Proceedings of the IEEE Conference on Computer Vision and Pattern Recognition (CVPR, 2015)*.

[7] F. Engels, P. Heidenreich, A. M. Zoubir, F. K. Jondral, and M. Wintermantel, “Advances in automotive radar: A framework on computationally efficient high-resolution frequency estimation,” *IEEE Signal Processing Magazine*, 2017.

[8] M. Meyer and G. Kuschk, “Automotive radar dataset for deep learning based 3d object detection,” *2019 16th European Radar Conference (EuRAD)*, pp. 129–132, 2019.

[9] M. Cordts, M. Omran, S. Ramos, T. Rehfeld, M. Enzweiler, R. Benenson, U. Franke, S. Roth, and B. Schiele, “The cityscapes dataset for semantic urban scene understanding,” in *Proceedings of the IEEE Conference on Computer Vision and Pattern Recognition (CVPR)*, 2016.

[10] G. Neuhold, T. Ollmann, S. Bulò, and P. Kotschieder, “The mapillary vistas dataset for semantic understanding of street scenes,” in *Proceedings of the IEEE International Conference on Computer Vision (ICCV)*, 2017.

[11] G. Ros, L. Sellart, J. Materzynska, D. Vazquez, and A. Lopez, *The SYNTHIA Dataset: A large collection of synthetic images for semantic segmentation of urban scenes*. in CVPR, 2016.

[12] A. Gaidon, Q. Wang, Y. Cabon, and E. Vig, *Virtual worlds as proxy for multi-object tracking analysis*. in CVPR, 2016.

[13] A. Dosovitskiy, G. Ros, F. Codevilla, A. Lopez, and V. Koltun, “CARLA: An open urban driving simulator,” ser. *Proceedings of Machine Learning Research*, vol. 78. PMLR, 13–15 Nov 2017, pp. 1–16. [Online]. Available: <http://proceedings.mlr.press/v78/dosovitskiy17a.html>

[14] A. Shrivastava, T. Pfister, O. Tuzel, J. Susskind, W. Wang, and R. Webb, “Learning from simulated and unsupervised images through adversarial training,” in *Proceedings of the Conference on Computer Vision and Pattern Recognition*, 2017.

[15] M. Bühren and B. Yang, “Automotive radar target list simulation based on reflection center representation of objects,” in *in Proc. Intern. Workshop on Intelligent Transportation (WIT, 2006*, pp. 161–166.

[16] Z. Shuqing, *Performance Evaluation of Automotive Radars Using Carrier-Phase Differential GPS*. in *IEEE Transactions Instrumentation and Measurement*, 2010.

[17] S. Schult, “Generierung von synthetischen 77-ghz-radarrohsignalen aus lidar-& kameradatensätzen für die evaluation von objektklassifikatoren in automive-radaranwendungen,” Master’s thesis, Masters Thesis, University of Applied Science Gelsenkirchen Bocholt Recklinghausen, 2018.

[18] B. Major, D. Fontijne, A. Ansari, R. T. Sukhavasi, R. Gowaikar, M. Hamilton, S. Lee, S. Grzegorczyk, and S. Subramanian, “Vehicle detection with automotive radar using deep learning on range-azimuth-doppler tensors.” *IEEE/CVF International Conference on Computer Vision Workshop (ICCVW)*, 2019.

[19] A. P. Sligar, *Machine Learning-Based Radar Perception for Autonomous Vehicles Using Full Physics Simulation*. IEEE Access, 2020.

[20] L. Wang, C. Anklam, and F. Baumgaertner, “Labelling of data for classification with automotive radar sensors,” in *automotive Forum of European Microwave Integrated Circuit Conference (EuMIC)*, 2019.

[21] L. Wang, T. Chen, C. Anklam, and B. Goldluecke, “High dimensional frustum pointnet for 3d object detection from camera, lidar, and radar,” in *Proceedings of the IEEE Intelligent Vehicles Symposium (IV)*, 2020.

[22] V. Stabilito, “Phase-comparison monopulse radar,” *United States US US3167765A*, 1961.

[23] H. Krim and M. Viberg, “Two decades of array signal processing research,” *IEEE Signal Processing Magazine*, vol. 13, 1996.

[24] M. Gardill, J. Fuchs, C. Frank, and R. Weigel, “A multi-layer perceptron applied to number of target indication for direction-of-arrival estimation in automotive radar sensors,” in *Proceedings of the IEEE 28th International Workshop on Machine Learning for Signal Processing (MLSP)*, 2018.

[25] J. Fuchs, R. Weigel, and M. Gardill, “Single-snapshot direction-of-arrival estimation of multiple targets using a multi-layer perceptron,” in *Proceedings of the 2019 IEEE MTT-S International Conference on Microwaves for Intelligent Mobility (ICMIM)*, 2019.

[26] ———, “Model Order Estimation using a Multi-Layer Perceptron for Direction-of-Arrival Estimation in Automotive Radar Sensors,” in *Proceedings of the 2019 IEEE Topical Conference on Wireless Sensors and Sensor Networks (WiSNet)*, 2019.

[27] Velodyne LiDAR, “Ultra puck,” *datasheet*, vol. 27, July 2020. [Online]. Available: http://www.mapix.com/wp-content/uploads/2018/07/63-9378_Rev-D_ULTRA-Puck_VLP-32C_Datasheet_Web.pdf

[28] FirstSensor, “Blue next network digital camera e4p,” *datasheet*. [Online]. Available: https://www.first-sensor.com/cms/upload/datasheets/DS_Blue_Next_DC3C-1-E4P.pdf

[29] GeneSys Elektronik GmbH, “Adma,” 2020, *datasheet*. [Online]. Available: https://www.genesys-offenburg.de/index.php?eID=tx_securedownloads&p=110&u=0&g=0&t=1595915060&hash=ccb5d292bcfc9f7f7492e7b888d0a8d6ca71736f&file=fileadmin/user_upload/ProdDescr_ADMA_rel_05.2019.pdf

[30] J. Levinson and S. Thrun, *Unsupervised Calibration for Multi-beam Lasers*. in *Experimental Robotics*, 2014.

[31] U. Kuehnau, “Sensor development for autonomous driving,” *Automotive Radar Sensors for Semi-Automatic and Autonomous Driving and Parking Systems*, IWPC Wolfsburg, Tech. Rep., 2017.

[32] S. Schneider, M. Himmelsbach, T. Luettel, and H. Wuensche, “Fusing vision and lidar – synchronization, correction and occlusion reasoning,” in *Proceedings of the IEEE Intelligent Vehicle Symposium*, 2010.

[33] H. Caesar, V. Bankiti, A. H. Lang, S. Vora, V. E. Liou, Q. Xu, A. Krishnan, Y. Pan, G. Baldan, and O. Beijbom, “nuscenes: A multimodal dataset for autonomous driving,” March 2019, [cs.LG].

[34] P. Merriaux, Y. Dupuis, R. Boutteau, P. Vasseur, and X. Savatier, “Lidar point clouds correction acquired from a moving car based on can-bus data,” June 2017, [cs.RO].

[35] W. Ma, S. Wang, R. Hu, Y. Xiong, and R. Urtasun, “Deep rigid instance scene flow,” in *ICCV*, April 2019.

[36] Tensorflow, “Detection model zoo,” 2020, *GitHub repository*. [Online]. Available: https://github.com/tensorflow/models/blob/master/research/object_detection/g3doc/detection_model_zoo.md

[37] Z. Yin, T. Darrell, and F. Yu, “Hierarchical discrete distribution decomposition for match density estimation.” *IEEE Conference on Computer Vision and Pattern Recognition (CVPR)*, 2019.

[38] J. Diebel and S. Thrun, “An application of Markov random fields to range sensing,” in *proceedings of Advances in Neural Information Processing Systems (NIPS)*, 2006.

[39] A. Harrison and P. Newman, “Image and sparse laser fusion for dense scene reconstruction,” in *Proceedings of the Field and Service Robotics*, 2009.

[40] C. Schröder, *System Design of an Array Antenna Radar with a Rapid Chirp Waveform*, ser. Berichte aus der Elektrotechnik. Shaker Verlag, 2013. [Online]. Available: <https://books.google.de/books?id=TyKTngEACAAJ>

[41] M. Ester, H. Kriegel, J. Sander, and X. Xu, “A density-based algorithm for discovering clusters in large spatial databases with noise,” in *Proceedings of the International Conference on Knowledge Discovery and Data (KDD)*, 1996.

[42] M. M. and, and H. Wallentowitz. *Dynamik der Kraftfahrzeuge*: Springer, 2004.

[43] T. Lindeberg, “Scale-space theory: A basic tool for analysing structures at different scales,” *Journal of Applied Statistics*, vol. 21, no. 2, pp. 224–270, 1994.

[44] T. Zhou, M. Brown, N. Snavely, and D. Lowe, *Unsupervised Learning of Depth and Ego-Motion from Video*. in *Proceedings of the IEEE Conf. on Computer Vision and Pattern Recognition (CVPR)*, 2017.

[45] M. Jaderberg, K. Simonyan, A. Zisserman, and K. Kavukcuoglu, “Spatial transformer networks,” in *Proceedings of the Advances in Neural Information Processing Systems (NIPS)*, 2015.

[46] M. Zhao, T. Li, M. Alsheikh, Y. Tian, H. Zhao, A. Torralba, and D. Katabi, “Through-wall human pose estimation using radio signals,” in *Proceedings of the IEEE Computer Society Conference on Computer Vision and Pattern Recognition (CVPR)*, 2019.

[47] M. Menze and A. Geiger, “Object scene flow for autonomous vehicles.” *IEEE Conference on Computer Vision and Pattern Recognition (CVPR)*, 2015.

[48] C. Grimm, T. Breddermann, R. Farhoud, T. Fei, E. Warsitz, and R. Haeb-Umbach, “Hypothesis test for the detection of moving targets in automotive radar,” in *2017 IEEE International Conference on Microwaves, Antennas, Communications and Electronic Systems (COMCAS)*, 2017, pp. 1–6.

[49] C. Grimm, R. Farhoud, T. Fei, E. Warsitz, and R. Haeb-Umbach, “Detection of moving targets in automotive radar with distorted ego-velocity information,” in *2017 IEEE Microwaves, Radar and Remote Sensing Symposium (MRRS)*, 2017, pp. 111–116.

[50] L. Mesow, “Multisensorielle datensimulation im fahrzeugumfeld für die bewertung von sensorfusionsalgorithmen,” Ph.D. dissertation, Technical University Chemnitz, 2006.

- [51] S. Heuel, "Fußgängererkennung im straßenverkehr mit 24ghz radarsensoren," Ph.D. dissertation, Hamburg University of Technology, 2013.
- [52] Y. Yang, J. Lei, W. Zhang, and C. Lu, "Target classification and pattern recognition using micro-doppler radar signatures," International Conference on Software Engineering, Artificial Intelligence, Networking and Parallel/Distributed Computing, 2006.
- [53] I. Woodhouse, *Introduction to Microwave Remote Sensing*. Boca Raton, USA: CRC, 2006.
- [54] T. Lin, P. Goyal, R. Girshick, K. He, and P. Dollár, "Focal loss for dense object detection," August 2017, [cs.CV].



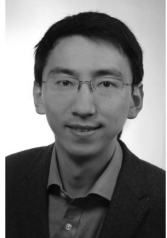
Ridha Farhoud Ridha Farhoud received the Dipl.-Ing. degree in electrical engineering and the Dr.-Ing. degree from the Leipzig University in Hannover in 1997 and 2009, respectively. From 1998 to 2010, he worked as research engineer at the „Institut für Informationsverarbeitung“ (information processing) in Hannover. He was involved in several projects related to Synthetic Aperture Radar, Image Interpretation and low bit rate video coding. In 2010, he joined Hella KGaA Hueck & Co. He is currently a member of the Radar Signal Processing and Signal Validation Department at HELLA GmbH & Co. KGaA, Lippstadt, Germany



Christopher Grimm received the B. Eng. degree in automotive engineering from University of Applied Science and Arts Dortmund, Germany, in 2013, and the M. Sc. in mechanical engineering from Technical University of Braunschweig, Germany, in 2015. Since 2016 he is pursuing the Dr.-Ing. degree in electrical engineering with the Department of Communications Engineering, University of Paderborn, Germany and HELLA GmbH & Co. KGaA, Lippstadt, Germany. Since 2020, he is working as a development engineer at HELLA GmbH & Co. KGaA where he is responsible for the development of artificial intelligence based radar signal processing algorithms. His research interests are automotive radar signal processing, machine learning and computer vision.



Tobias Breddermann Tobias Breddermann received the Dipl.-Ing. degree in electrical engineering and the Dr.-Ing. degree from RWTH Aachen University, Aachen, Germany, in 2007 and 2013, respectively. From 2007 to 2013, he was with the Institute of Communication Systems and Data Processing at RWTH Aachen University. In 2013, he joined HELLA GmbH & Co. KGaA. His research interests include radar singal processing, advanced DoA estimation and target seperation.



Tai Fei (S'12-M'19) received the B.Eng. degree in telecommunication engineering from Shanghai Maritime University, Shanghai, China, in 2005 and the Dipl.-Ing. and Dr.-Ing. degrees in electrical engineering and information technology from Darmstadt University of Technology (TUD), Darmstadt, Germany, in 2009 and 2014, respectively. From 2009 to 2012, he worked as a Research Associate with the Institute of Water-Acoustics, Sonar-Engineering and Signal-Theory at Hochschule Bremen, Bremen, Germany, in collaboration with the Signal Processing Group at TUD, Darmstadt, Germany, where his research interest was the detection and classification of underwater mines in sonar imagery. From 2013 to 2014, he worked as a Research Associate with the Center for Marine Environmental Sciences at University of Bremen, Bremen, Germany. Since 2014, has been working as a development engineer at HELLA GmbH & Co. KGaA, Lippstadt, Germany, where he is mainly responsible for the development of reliable signal processing algorithms for automotive radar systems.



Reinhold Haeb-Umbach is a professor of Communications Engineering at Paderborn University, Germany. He holds a Dr.-Ing. degree from RWTH Aachen University, and has a background in speech research both in an industrial and academic research environment. His main research interests are in the fields of statistical signal processing and pattern recognition, with applications to speech enhancement, acoustic beamforming and source separation, as well as automatic speech recognition and unsupervised learning from speech and audio. He has more than 200 scientific publications, and recently co-authored the book Robust Automatic Speech Recognition – a Bridge to Practical Applications (Academic Press, 2015). From 2015 – 2020 he is/has been a member of the IEEE Signal Processing Society Speech and Language Technical Committee. He is a fellow of the International Speech Communication Association (ISCA), class of 2015.



Ernst Warsitz received the Dipl.-Ing. and Dr.-Ing. degrees in electrical engineering from Paderborn University, Paderborn, Germany, in 2000 and 2008, respectively. He joined the Department of Communications Engineering of the University of Paderborn in 2001 as a Research Staff Member, where he was involved in several projects relating to single- and multi-channel speech processing and automated speech recognition. From 2007 he worked as a development engineer at HELLA GmbH & Co. KGaA, Lippstadt, Germany, in the field of signal

processing algorithms for automotive radar systems. He is currently the head of the Radar Signal Processing and Signal Validation Department at HELLA GmbH & Co. KGaA, Lippstadt, Germany